NUMERICAL ESTIMATION OF ENHANCEMENT FACTOR OF SILVER NANOWIRE FILTER FOILS AS SERS SUBSTRATES

A THESIS SUBMITTED TO
THE GRADUATE SCHOOL OF NATURAL AND APPLIED SCIENCES
OF
MIDDLE EAST TECHNICAL UNIVERSITY

BY

SELEN YÜKSEL

IN PARTIAL FULFILLMENT OF THE REQUIREMENTS
FOR
THE DEGREE OF MASTER OF SCIENCE
IN
MICRO AND NANOTECHNOLOGY

JANUARY 2023

Approval of the thesis.:

NUMERICAL ESTIMATION OF ENHANCEMENT FACTOR OF SILVER NANOWIRE FILTER FOILS AS SERS SUBSTRATES

submitted by **SELEN YÜKSEL** in partial fulfillment of the requirements for the degree of **Master of Science** i**n Micro and Nanotechnology, Middle East Technical University** by,

Prof. Dr. Halil Kalıpçılar
Dean, Graduate School of **Natural and Applied Sciences**

Prof. Dr. Deniz Üner
Head of the Department, **Micro and Nanotechnology** _____

Prof. Dr. Alpan Bek
Supervisor, **Physics, METU** _____

Prof. Dr. Mehmet Emre Taşgın
Co-Supervisor, **Nuclear Sciences, Hacettepe University** _____

Examining Committee Members:

Assoc. Prof. Dr. Tahir Çolakoğlu
Physics Engineering, Ankara University

Prof. Dr. Alpan Bek
Physics, METU _____

Prof. Dr. Halil Berberoğlu
Physics, Ankara Hacı Bayram Veli University

Assoc. Prof. Dr. Görkem Günbaş
Chemistry, METU _____

Assoc. Prof. Dr. Emre Yüce
Physics, METU _____

Date: 26.01.2023

I hereby declare that all information in this document has been obtained and presented in accordance with academic rules and ethical conduct. I also declare that, as required by these rules and conduct, I have fully cited and referenced all material and results that are not original to this work.

Name Last name : Selen Yüksel

Signature :

ABSTRACT

NUMERICAL ESTIMATION OF ENHANCEMENT FACTOR OF SILVER NANOWIRE FILTER FOILS AS SERS SUBSTRATES

Yüksel, Selen
Master of Science, Micro and Nanotechnology
Supervisor : Prof. Dr. Alpan Bek
Co-Supervisor: Prof. Dr. Mehmet Emre Taşgın

January 2023, 75 pages

Surface Enhanced Raman Scattering (SERS) is a surface-sensitive vibrational spectroscopy technique. Highly SERS-active substrates made of nanostructured noble metals have been widely investigated owing their activity to the formation of localized surface plasmon resonances, hotspots, where electromagnetic field is amplified by several orders of magnitude locally. Silver and gold are the two most studied noble metals due to their especially low losses and hence high enhancement factors (EF). Gold is chemically stable which is ideal against aging however silver possesses lower losses. Therefore, despite their high EF, silver nanostructures are useful only with a suitable protective coating layer. As an analytic tool, use of SERS has been proven in detection of trace molecules countless times. However, its use has been limited in the detection of larger scale materials including biological pathogens. Recently thick and dense AgNW networks in the form of filter foils have been developed for this aim with the dual function of filtering the pathogens from liquids and also acting as a SERS substrate. In this thesis work, it is aimed to estimate the expected Raman EF of AgNWs using numerical simulations. Finite-difference time-domain (FDTD) based Maxwell solver is used for its versatility, availability and well-established literature in this work. In our approach EF of complex AgNW

networks is estimated using FDTD method by dividing them into sub-systems represented by two mutually parallel- and cross-oriented AgNWs. Simulations are conducted to assess the dependence of EF to distance between parallel and crossed wires, and to protective dielectric coating thickness, and the polarization angle. Calculated estimates of EF values are found to range from 10^4 to 10^7 which agree very well with the experimental studies carried out in our research group. This is a surprising result considering the simplicity of our approach against the complexity of the actual AgNW network.

Keywords: Surface Enhanced Raman Scattering, Enhancement Factor, Silver, Nanowire, Filter

ÖZ

SERS YÜZEYLERİ OLARAK GÜMÜŞ NANOTEL FİLTRE FOLYOLARININ ARTIRIM FAKTÖRÜNÜN SAYISAL HESABI

Yüksel, Selen
Yüksek Lisans, Mikro ve Nanoteknoloji
Tez Yöneticisi:Prof. Dr. Alpan Bek
Ortak Tez Yöneticisi: Prof. Dr. Mehmet Emre Taşgın

Ocak 2023, 75 sayfa

Yüzey Artırımlı Raman Spektroskopisi (SERS), yüzeye duyarlı bir titreşim spektroskopisi yöntemidir. Yüksek düzeyde SERS aktif alttaşlara, SERS'e özgü iyileştirme sağlayan yüzey plazma rezonansının oluşumu nedeniyle metalik nano yapılar aracılığıyla çalışılır. Nano ölçekte, soy metal yapılar, elektromanyetik alanın yoğunluğunu bölgesel artırarak sinyalin görünürlüğünü arttırır. Gümüş ve altın, düşük kayıpları ve yüksek geliştirme faktörleri (EF) nedeniyle en çok çalışılan soy metallerdir. Altın kimyasal olarak kararlıdır ve yaşlanmaya karşı idealdir, ancak gümüşün kayıpları daha düşüktür. Yüksek EF'lerine rağmen, gümüş nanoyapılar yalnızca uygun koruyucu kaplama tabakası ile kullanışlıdır. Analitik bir araç olarak SERS'in kullanımı eser moleküllerin tespitinde sayısız kez kanıtlanmıştır ancak biyolojik patojenler gibi büyük ölçekli malzemelerin tespitinde kullanımı sınırlıdır. Son zamanlarda, filtre folyoları şeklindeki kalın ve yoğun AgNW ağları, patojenleri sıvılardan filtreleme ve SERS substratı olarak işlev görme ikili işlevi ile geliştirilmiştir. Bu tez çalışmasında, AgNW'lerin beklenen Raman EF'sinin sayısal simülasyonlar kullanılarak tahmin edilmesi amaçlanmaktadır. Bu çalışmada çok yönlülüğü, kullanılabilirliği ve köklü literatürü nedeniyle zamanda sonlu farklar (FDTD) tabanlı Maxwell çözücü kullanılmıştır. Yaklaşımımızda, karmaşık AgNW

ağlarının EF'si, FDTD yöntemi kullanılarak, karşılıklı olarak paralel ve çapraz yönlü iki AgNW tarafından temsil edilen alt sistemlere bölünerek tahmin edilmektedir. EF'nin paralel ve çapraz teller arasındaki mesafeye, koruyucu dielektrik kaplama kalınlığına ve polarizasyon açısına bağımlılığını değerlendirmek için simülasyonlar yapılmıştır. Hesaplanan EF değerlerinin 10^4 ila 10^7 arasında olduğu ve bu sonuçların araştırma grubumuzda yürütülen deneysel çalışmalarla çok iyi bir uyum içinde olduğu bulunmuştur. Bu, gerçek AgNW ağının karmaşıklığına karşı yaklaşımımızın basitliği düşünüldüğünde şaşırtıcı bir sonuçtur.

Anahtar Kelimeler: Yüzey Artırımlı Raman Spektroskopisi, Artırım Faktörü

To my family

ACKNOWLEDGMENTS

I would like to express my deepest gratitude to my supervisor Assoc. Dr. Alpan Bek for his guidance, understanding and support through my MS study. As Carl Sagan says “Somewhere, something incredible is waiting to be known.”. The enthusiasm of Dr. Bek always influenced me to never give up, to experience more and to have a passion for learning.

I am deeply thankful to my co-supervisor Prof. Dr. Mehmet Emre Taşgın, Dr. Zafer Artvin, İbrahim Can Küçükyılmaz, Görkem Gökçen and Arda Kandemir for their cooperation and guidance through simulations.

I would like to thank to my huge and loving Yüksel, Eryiğit, Şenol, Erdem and Erdemir families for their support. I feel deeply thankful to my parents, Tevfik Yüksel, Zübeyde Yüksel, and my sister, Sezen Yüksel, for being there whenever I need, simply loving me for who I am and guiding me to be my best version.

I would like to thank İlker Kütük, Ramona Davoudnezhad, Ateşcan Aliefendioğlu, Ezgi Abacıoğlu, Nardin Avişan Taştekin, Özge Demirtaş, Tuğçe Odabaş, Hilal Pat, Simge Doğan, Ece Selin Böncü, Gözde Varürer, Deniz Can, Begüm Beril İncecik, Doğancan Tigan, Şeyma Koç, Sedanur Toraman, Sevinç Yüksel, Kübra Cerit, Bleda Gülsen, Orkun Erdenay Duran, Öznur Uysal Yıldız, Çağatay Kaya, Oğuzcan Taşdemir, İrem Öztürk, Cenk Sumbas, Gökşen Bilir, Burak Tarkan, Diyar Güldoğan, Koray Alper, Yunus Emre Sert, Tuğba Hacıefendioğlu, Büşra Bilmez, Teoman Cem Katoğlu, Melih Kara, Umut Demirbozan , Zafer Coruhlu, Yusuf Yılmaz, Meliz Koral, Elvan Eker, Tuğçe Kaya Balaman, Servet Aybar, Nika, AST, The Studio by MUCSS Team and Fight Club Team for their unconditional love and support. When you have a great team and motivation success is inevitable.

Last but not least, I would like to thank Prof. Dr. Raşit Turan, Prof. Dr. Serhat Çakır, Prof. Dr. Enver Bulur, Prof. Dr. Ayşe Karasu, Prof. Dr. Altuğ Özpineci, Prof. Dr.

Bayram Tekin and Assoc. Prof. Dr. Hande Toffoli for the past experiences that taught me a lot in my academic life.

This thesis work has been supported by TÜBİTAK under grant nr. 119N413.

TABLE OF CONTENTS

LIST OF TABLES

TABLES

LIST OF FIGURES

FIGURES

LIST OF ABBREVIATIONS

ABBREVIATIONS	
AgNW	Silver Nanowire
EF	Enhancement Factor
EM	Electromagnetic
LSPR	Localized Surface Plasmon Resonance
MNP	Metal Nanoparticle
nm	Nanometer
SEM	Scanning Electron Microscope
SERS	Surface Enhanced Raman Scattering
SP	Surface Plasmon
SPP	Surface Plasmon Polariton

CHAPTER 1

INTRODUCTION

Surface Enhanced Raman Scattering (SERS) provides substantial vibrational spectroscopic information rendering various applications in the fields of biology, medicine, electrochemistry, materials science and in other domains possible. Plasmonic optical biosensors, highly sensitive bio-detection in biomedicine, optical cancer screening, label-free molecular imaging of live cells, graphene-based nanoplatforms for biosensing, TiO_2 based substrates and quantum dots for ultrasensitive detection of organic pollutants are some instances of specific fields of SERS studies. SERS, a localized surface plasmon (LSP) application, makes use of the enhanced local fields due to plasmon excitation in the nanoparticles. SERS remarkably enhances the weak signal of Raman scattering from a substance. The large enhancement provided by SERS makes even the detection of single molecules possible allowing the characterization of the molecules in the neighborhood of plasmonic structures [1]. The discovery of SERS emerged from the studies of Fleischmann et al. during measurements of the Raman scattering of pyridine to be discussed in the following brief literature review.

In 1930, Chandrasekhara Venkata Raman was awarded the Nobel Prize in Physics for the discovery of phenomena covering the inelastic scattering of photons by matter where an exchange of energy and a change in the direction of light appears, later named after Raman. Raman scattering delivers information about vibrations within a molecule. Conceptualization of Raman Spectroscopy became prominent subsequent to the invention of lasers as severe excitation sources to amplify the effect and ease the detection of the scattered light. Raman Spectroscopy namely, a non-destructive chemical analysis technique provided comprehensive information about chemical structure, phase, crystallinity and molecular interactions [2].

An experimental demonstration of SERS effect was first carried out by Fleischmann, Hendra and McQuillan at the Department of Chemistry of University of Southampton, UK in 1974 followed by the publication of "Raman Spectra of Pyridine Adsorbed at a Silver Electrode" in Chemical Physics Letters. Raman spectroscopy was initially utilized for conducting a study on the role of adsorption at electrodes. Cary 82 Raman Spectrometer utilized at $2cm^{-1}$ slits having 5000 counts/sec unreduced sensitivity, 100 mW Argon Ion Laser operating at 514.5 nm, a peripheral electrode consisting of a platinum wire, a principal electrode involving a Johnson Matthey Specpure silver rod encased in polytetrafluoroethylene, a Chemical Electronics potentiostat and a Chemical Electronics waveform generator is used for the investigation. An aqueous solution comprising of 0.1 M analytical grade KCl and 0.05 M pyridine in contact with silver electrode is prepared and following that the electrode experienced cyclic linear potential sweeping for 15 minutes at 0.5V sec-1 between 200mW and 300 mW. The surface area is remarked to increase by a factor no fewer than 10. As a consequence, the measurements of Raman scattering of pyridine, a strong Raman scatterer, on rough silver electrodes yield an enhancement due to a surface-area effect [3].

At a succeeding time, Jeanmaire and Van Duyne identified a Raman intensity enhancement mechanism that allows the observations of the spectra of molecules adsorbed on an electrode surface concurrently with Albrecht and Creighton. While concluding the investigation two points of discussion arose. First point of discussion is resonance Raman scattering is assumed to be induced through interaction with surface plasmons and the second point of discussion is the normal Raman scattering cross section of the adsorbed pyridine molecules is presumed to be enhanced by the tremendously large interfacial electric field gradient (10^6 to 10^7 V cm^{-1}) in the double layer region. The available experimental data was not sufficient to identify the standing hypothesis. Nevertheless, Jeanmaire and Van Duyne presented the increase of electromagnetic field as the reason of enhancement mechanism and suggested enhancement factors (EF's) ranging from 10^5 to 10^6 which was also proposed by Albrecht and Creighton simultaneously [4]. Raman spectra of pyridine adsorbed at a

pre-roughened silver electrode by electrochemical cycling have been released earlier by Fleischmann, Hendra and McQuillan. Albrecht and Creighton reported that the Raman spectra of pyridine at a silver electrode after a single oxidation-reduction cycle and especially when evidenced throughout and directly after the cycle are exceptionally intense. Furthermore, the relation with plasmon excitation was indicated by Albrecht and Creighton as a resonant Raman effect involving plasmon excitation referring to Philpott's studies comprising the quantum theory of the coupling of excited molecules to the surface plasmon modes of a metal, the Raman effect and resonance energy transfer between identical molecules [5], [6].

Subsequently, Moskovits declared the correlation of SERS intensities with enhanced fields emerging from localized surface plasmons in nanostructured metals. The study was based on the resonant excitations of conduction electron resonances in adsorbate covered metal bumps on the surface leading to show abnormal intensities up, followed by formation of a two-dimensional layer exhibiting a collective resonance at a frequency varying upon the bump density [7]. In 1997, Kneipp and collaborators made use of immensely large cross sections (10^{-17}-10^{-16} cm^2/molecule) and accomplished the first observation of a single molecule Raman scattering, the spectra of a single crystal violet molecule in aqueous colloidal silver solution [8].

The theory behind SERS being a sensitive analytical technique, the choice and enhancement of substrates and related interdisciplinary applications have been studied and various publications have been made yielding the consensus among scientists that Enhancement Factor (EF) is incorporation of an electromagnetic enhancement due to plasmon excitation in metal particles used as SERS substrates and a chemical enhancement due to the target molecules that are free to transfer electrons to and from the metal particles in both ground and excited states.

The Localized Surface plasmon resonance is the collective oscillation of conduction band electrons in metal nanoparticles stimulated by incident light. The interaction of an electromagnetic wave and a bent metallic surface yields in a restoring force on oscillating electrons. As a consequence, the resonance leads to amplification of the

field on the surface of the metallic nanostructure. The electromagnetic field enhancement on the surface of a spherical metallic nanostructure is described by Mie Theory giving information about the relation of polarizability with the radius of the nanoparticle, the permittivity of the metal, the resonance frequency and the permittivity of the surrounding medium. As the permittivity of the metal approaches to the resonance frequency, the polarizability hits its maximum value therefore the near-field electric field of the metallic nanostructure is enhanced. The localization of the electric field near the surface of the metal nanoparticle and the related enhancement factor may be modelled and calculated using Finite-Difference Time-Domain (FDTD) method [9], [10].

Silver metal-based SERS is promising due to large enhancement factors reaching 10^7 at silver plasmon resonance allowing satisfying detectivity levels. As mentioned above, SERS is favorable for the single molecule's detection but current practice is not adequate for larger structures such as pathogens. AgNW filter foils permits isolation of the pathogens while providing convenient SERS substrates. Furthermore, AgNW filter foils may lead to enhancement in detection of SERS based detectors due to their high-sensitivity and reproducibility. For the purpose of computing the enhancement factor (EF) numerical simulation is useful and most frequently used numerical simulations are FDTD simulations that yield scattering enhancement.

In this thesis, the SERS modelling of various Ag nanowire foil configurations will be studied, in this context the enhancement factors will be calculated.

CHAPTER 2

THEORY

2.1 Rayleigh Scattering

Scattering of light is defined as departure of electromagnetic waves from the path of the incident wave by the imperfections in the scattering medium and the partial reemission of involved energy in various directions [12].

Interaction of an electromagnetic wave with a particle or molecule leads to oscillatory motion of electrons so to an oscillating electric field creating the corresponding oscillating dipole, μ, defined as,

$$\mu = \alpha E \tag{2.1}$$

where α is polarizability.

When the incident radiation and the oscillating dipole radiates at the same frequency, the phenomenon is called Rayleigh scattering. Rayleigh scattering is an elastic effect so the light does not gain or lose energy throughout the scattering process which is greatly wavelength dependent ($\propto\lambda^{-4}$).

Different molecules scatter with different efficiencies due to having different number of electrons. Rayleigh scattering law is expressed as [13],

$$P = \frac{e^2\omega^4 r_0^2}{12\pi\varepsilon_0 c^3} \tag{2.2}$$

On the grounds of this, the oscillating dipoles radiate more energy in the shorter-wavelength region of the visible spectrum than in the longer-wavelength region.

To have further information about the polarization of the scattered radiation, molecules scatter no energy along the dipole axis so as the charges oscillate along y-

axis, there exists no radiation in the same direction. Hence, at right angles with the beam direction, the scattered light is linearly polarized. Controlled scattering of light from the active media that is a cluster of atoms/molecules that may bring out electromagnetic radiation due to stimulated emission, contributes to research areas in nonlinear optics unlike ordinary polarization by scattering. Stimulated Raman and Rayleigh scattering are significant examples of aforementioned controlled scattering [12].

2.2 Raman Scattering

Raman scattering is the inelastic scattering of photons where the frequency of the scattered photon varies from the frequency of the incident photon. In other words, there is an exchange of energy as the scattering process takes place. Consequently, there is a change in the wavelength.

Raman scattering provides information about vibrations within a molecule. The discussion may be elaborated by classifying Raman scattering in two sub-types that are Stokes Raman scattering and Anti-Stokes Raman scattering.

2.2.1 Stokes Raman Scattering

Stokes Raman scattering arises when a molecule or an atom at the ground state is excited to a virtual state and return to a higher energy state so the energy of the scattered photon is below the energy of the incident photon. The molecule does not relax back to the ground state so the frequency of the scattered photon is reduced compared to the incident photon.

2.2.2 Anti- Stokes Raman Scattering

Anti-Stokes Raman scattering emerges when a molecule or an atom in the vibrational state is relaxed to ground state where the energy of the scattered photon is larger than

the initial photon. The molecule relaxes back to the ground state so the frequency of the scattered photon is increased compared to the incident photon.

The intensity of Raman scattering is low however among Stokes and Anti-Stokes Raman scatterings the more intense scattered radiation comes up from Stokes Raman scattering due to the fact that molecules are more likely to be in the ground state without the influence of the absorption of radiation [15]. In brief, the vibrational energy of the final state is higher in the Stokes Raman scattering, lower in Anti-Stokes Raman scattering as indicated in Figure 2.1 and the same in Rayleigh Scattering.

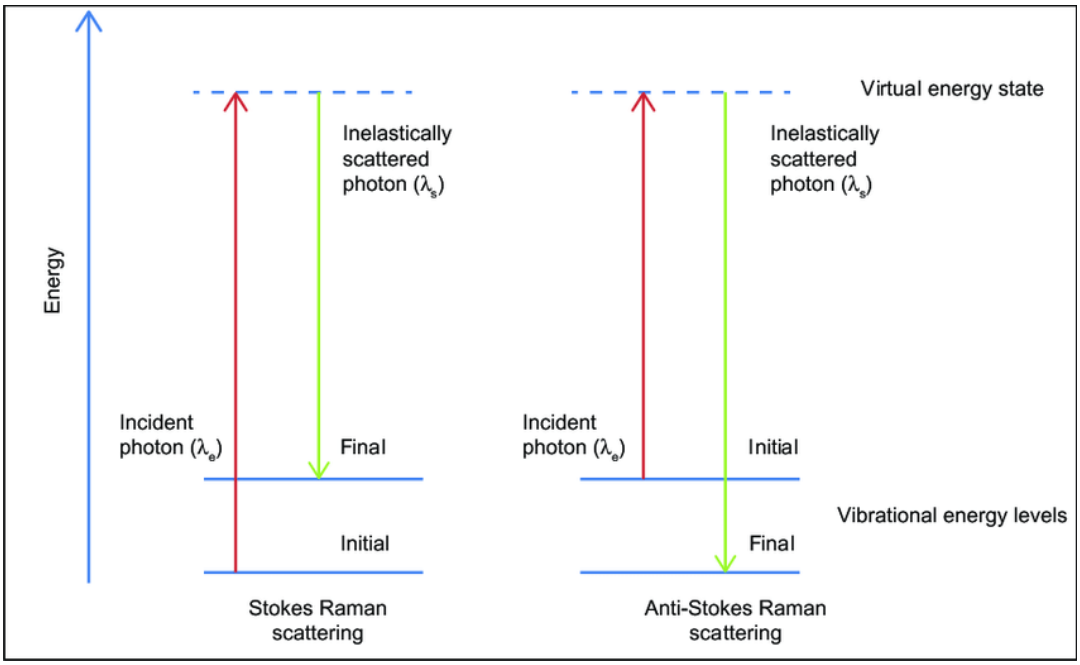

Figure 2.1 Schematic showing the difference between Stokes and anti-Stokes Raman scattering [14].

2.3 Raman Spectroscopy

Raman spectroscopy is a non-destructive analytical technique used in the assessment of molecular vibrations and is compatible with IR spectroscopy. IR spectroscopy operates in the infrared region of the electromagnetic spectrum referring to the investigation of interaction of a molecule with infrared light. Raman spectroscopy is

associated with vibrational spectroscopy providing considerable information including molecular interactions, chemical structure and crystallinity upon the interaction of light with the chemical bonds within the material.

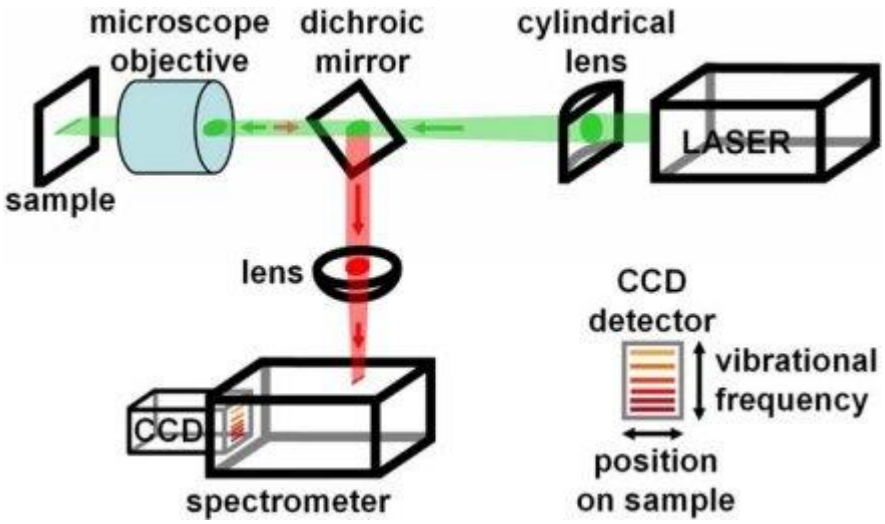

Figure 2.2 Schematic of Raman spectrometer [18].

A laser source is focused to a line on the sample which is named as slit scanning mode. A dichroic mirror filters the Raman- shifted light from the incident laser light. The Raman- shifted light is dispersed on a CCD detector that is a highly sensitive photon detector. In the slit-scanning mode it is possible to achieve many spectra along the CCD detector. Label-free sample investigation brings about the common usage of Raman microscopes although low scattering cross-section and diffraction-limited lateral resolution are current limitations of Raman spectroscopy that are being studied. Specifically, coherent anti-Stokes Raman spectroscopy grants the three-dimensional imaging of biological samples by improving z resolution in a shortened measurement period. Furthermore, tip-enhanced Raman spectroscopy makes use of the combination of scanning-probe microscopy with surface-enhanced Raman scattering in order to allow imaging below the optical diffraction limit by making use of the enhancement mechanism of surface-enhanced Raman scattering [18].

2.3.1 Raman Activity

IR and Raman spectroscopies probe distinct vibrational information of a molecule. The fundamental process of Raman spectroscopy is inelastic scattering meanwhile IR spectroscopy relies on an absorption process. The selection rule of IR spectroscopy demonstrates that vibrations are not allowed unless the molecular dipole moment changes during the vibration. For Raman spectroscopy as a molecule vibrates the polarizability, α, is supposed to change so the detection of the vibrations involving a variation in the polarizability can be detected [16]. Thus, the excitation of certain vibrational modes is allowed in Raman spectroscopy but are forbidden in IR spectroscopy. To sum up, a mode is specified to be Raman active when it involves a change in the polarizability of the molecule and is specified to be IR active when dipole moment changes. To express mathematically, a molecule is identified as Raman active if the polarizability tensor changes during the vibration as a function of normal coordinate of the molecule.

Electric field of an incident light interacting a molecule induces a dipole moment, $\boldsymbol{p}$, given in the following expression:

$$\boldsymbol{p} = \alpha \boldsymbol{E} + \frac{1}{2}\beta \boldsymbol{E}^2 + \frac{1}{6}\gamma \boldsymbol{E}^3 + \cdots \tag{2.3}$$

where $\boldsymbol{\alpha}$, $\boldsymbol{\beta}$ and $\boldsymbol{\gamma}$ are polarizability tensors [17].

The induced dipole moment in terms of vibrational frequencies is as indicated below:

$$\boldsymbol{p} = \boldsymbol{p}(v_0) + \boldsymbol{p}(v_0 + v_v) + \boldsymbol{p}(v_0 - v_v) \tag{2.4}$$

where the first term contributes to Rayleigh scattering, the second term corresponds to the anti-Stokes scattering and the third term represents the Stokes scattering.

Vibrations of homonuclear diatomic molecules are Raman active due to contribution of variations in the internuclear distance to the polarizability of the molecule. Vibrations of heteronuclear diatomic molecules are IR-active due to charge separation causing the dipole moment to change.

In order to identify the IR and Raman- active vibrational modes in complex molecules symmetry and group theory are applied which also provides information to predict the number of peaks in the related spectra. As a consequence, the IR and Raman selection rules are set. The vibrational modes with symmetry of x, y and z axes are IR- active whereas the modes with the symmetry of any binary products; xy, xz, yz, x^2, y^2, z^2, are Raman-active. For instance, for H_2O (a nonlinear triatomic molecule) two possible IR peaks and three possible Raman peaks are predicted via Group Theory.

2.3.2 Raman Shift

The interaction of the photons and the specimen molecules lead to emergence of Raman spectra that is defined as a "fingerprint" for the identification of materials. Conventionally, Raman intensity versus Raman shift is plotted in Raman spectrum. Raman shift is characterized as the difference of the Raman scattered frequency and the frequency of the incident light beam. The Raman shift is typically indicated in wavenumbers. In Raman scattering, a Stokes shift in wavelength arises as the photon transfers energy to the chemical bond. On the other hand, as the photon gains energy from the chemical bond, an anti-Stokes shift in wavelength appears.

Quiño et al. investigated in situ spatially resolved composition and concentration fields appearing inside silica aerogels during the supercritical drying process. One dimensional Raman spectroscopy is used for the assessment of the composition profiles inside the gel yielding the Raman spectrum measurement illustrated by Figure 2.3 that is an example of the Raman intensity versus Raman shift plot [19].

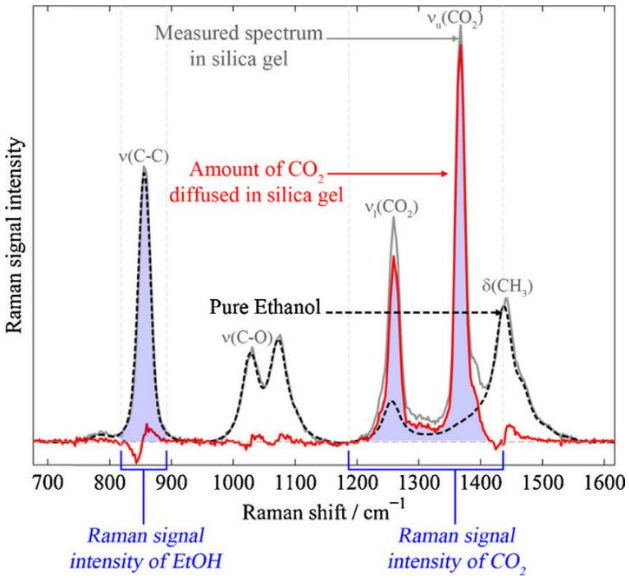

Figure 2.3 A Raman spectrum measured in silica gel at 318.15 K and 9.0 MPa (solid gray curve) [19].

In Figure 2.3, the dashed black curve represents the Raman spectrum of pure ethanol which is subtracted from the measured spectrum to observe the Raman signal contribution of pure CO_2 demonstrated by the solid red curve [19].

2.4 Diffraction Limit

Diffraction limit is a barrier that restricts the resolution of a system. Ernst Karl Abbe initially defined the fundamental limit as the smallest resolvable distance between two points using a conventional microscope is not allowed be smaller than half the wavelength of the imaging light [22].

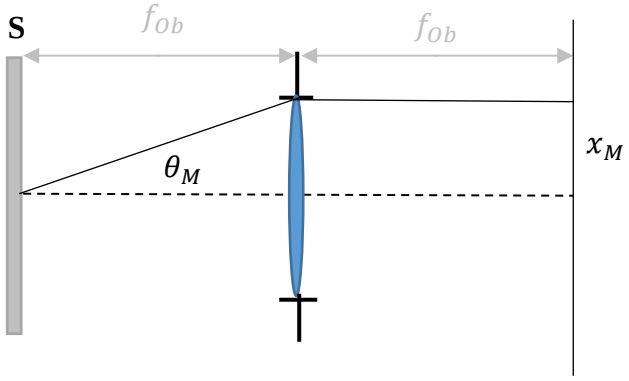

Figure 2.4 Frequency cut-off of a light microscope

In Figure 2.4, the apertures used in the microscope objective limit the maximum angle of scattered light by the specimen.

The cut-off frequency in 1D given by,

$$k_M = \frac{2\pi}{\lambda f_{Ob}} . x_M \tag{2.5}$$

where $\frac{x_M}{f_{Ob}} = \theta_M$ gives the maximum angle subtended by the entrance pupil from the specimen.

To derive Abbe's well-known formula for the resolution limit, correlation of the infinite resolution sample field and the image field is described by denoting the sample field as a Fourier transform of the field at the entrance pupil or equivalently denoting the image field as a Fourier transform of the exit pupil which are beyond the scope of this thesis. Abbe's diffraction limit is given by:

$$\Delta x \cong \frac{\lambda}{2n \sin \alpha} \tag{2.6}$$

The Rayleigh criterion for the diffraction limit to resolution states that two points are considered resolved when the maximum of one function overlaps with the second function at x_0=1.22π.

The resolution is obtained by solving the following equation:

$$2\pi \frac{r_M}{\lambda f_{Ob}} . \rho_0 = 1.22\pi \tag{2.7}$$

where $\frac{r_M}{f_{Ob}}$ represents the numerical aperture of the objective, *NA*.

Thus, the resolution defined by Rayleigh criterion is as indicated below:

$$\rho_0 = 0.61 \frac{\lambda}{NA} \tag{2.8}$$

where $\rho_0$is the distance between two points to be resolved, λ is the wavelength and *NA* indicates the numerical aperture of the microscope objective. This limit is a

fundamental limit not to be exceeded for far field optical applications including SERS.

In the field of Quantum Mechanics, Heisenberg's uncertainty principle asserts that the resolution limit defined by Rayleigh criterion is fundamental.

Heisenberg's uncertainty relation is expressed as:

$$\Delta x \geq \frac{1}{2\Delta k_i} \tag{2.9}$$

where Δx corresponds to the uncertainty in the position in a certain direction and $k_i = \sqrt{k_x^2 + k_y^2 + k_z^2}$ is wavevector of a photon.

Rayleigh diffraction limit description is attained by plugging $k_i = \frac{2\pi}{\lambda_i}$ into the equation 2.9 yielding the following relation:

$$\Delta x \geq \frac{\lambda}{4\pi} \tag{2.10}$$

The uncertainty in the position for far-field is

$$\Delta x \geq \frac{\lambda_i}{2\pi} \tag{2.11}$$

As an obstacle, Rayleigh diffraction limit prevents the detailed detection of certain properties of the nanoparticles for SERS applications. Nevertheless, there are some structures that can provide ways to exceed the diffraction limit, asserting techniques to direct light at the interface between the metal and a dielectric.

In 1928, near-field optical microscopy is proposed by Synge concerning near-field optical resolution overcoming the diffraction limit [23]. A nontransparent plate is placed in the vicinity of a substrate to achieve a high spatial resolution of spot beyond the diffraction limit of light by illuminating it from one side. It was indicated that resolution of acquired image had not been limited by wavelength of light but the size of the aperture.

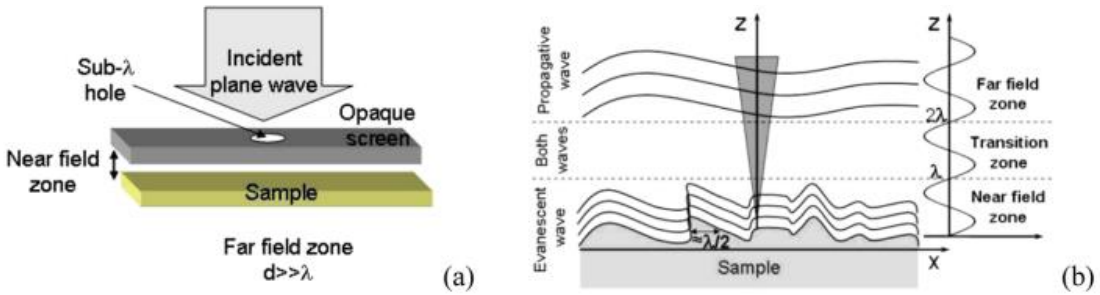

Figure 2.5 (a) Synge's representation of NSOM (b) Actual NSOM configuration [84].

In 1972, Ash and Nicholis achieved the first experimental demonstration of super resolution microscopy in the microwave frequencies. Ash and Nicholis attained an effective resolution of λ/60 by using 1.5 mm aperture [24]. In 1984, Lewis et al. made use of the identical configuration that was introduced by Synge [25]. A fabrication method for sub-wavelength aperture is released in 1981 by Murray et al. [26] using electron beam lithography. Nanoholes are processed in metallic or dielectric sheets with diameters to the extent of 50 nm showing high resolution capability.

In the interim, Pohl et al. developed the first NSOM, named as optical stethoscope, with a configuration similar to the currently used products [27]. Optical stethoscope was a combination of Synge's work with the concept of stethoscope which is a common medical tool yielding a groundbreaking optical resolution down to 50 nm. In 1986, Ferrell et al. [28] and Courjon et al. [29] independently proposed the Photon Scanning Tunnelling Microscope and Scanning Tunnelling Optical Microscope both rely on total internal reflection.

Progress in the probe-sample distance control is studied by several researchers. Betzig et al. introduced a distance regulation method making use of shear forces between the end of a near-field probe and the sample resulting in improvement of reliability and convenience of applications [30]. Ruiter et al. carried out experiments about the dynamics of a tuning fork shear-force feedback system, measuring amplitude and phase of the tuning fork oscillation in line with driving frequency and

tip-sample distance. The results indicated that resonance frequency of the tuning fork varies while approaching the sample [31]. An improved shear force microscope is studied by Antognozzi et al. to have a constant separation of the probe and the sample while scanning the surface of the sample [32]. Wetsel et al. used specific force sensors in scanned force probes and measured the displacement of the probes with the frequency and tip-sample separation during approach of the probe tip to the sample surface [33]. Lieberman et al. used a metal coated micropipette as a tunneling and near-field optical probe and investigated simultaneous scanning tunneling and optical near-field imaging [34]. Garcia-Parajo et al. used a gold coated single optical fiber as a tunneling and near-field optical probe to study tunneling regulation for simultaneous scanning tunneling microscope and SNOM [35]. The studies of interest yield electronic feedback development through the improvements in the probe-sample distance control.

Guiding fabrication processes are studied by Puygranier et al. via investigating chemical etching of optical fibre tips [36], by Valaskovic et al. via characterization and optimization in the fabrication of optical fiber near-field probes [38] and by Yakobson et al. via the fabrication of a tip by the widely used heating and pulling method in order to contribute to the spatial resolution [39]. The mentioned investigations about probe-sample distance, fabrication processes and related studies that are released subsequently influenced the improvements in the applications of NSOM. The progress in near-field lay the groundwork for investigation of plasmonics through NSOM for imaging plasmonic structures.

In the far field region, Fraunhofer diffraction concept applies when the light source is placed at infinite distance from the screen and the diffraction pattern is formed at considerably long distance from the diffracting object. For Fraunhofer diffraction the incident wave fronts on the obstacle are supposed to be plane. Fraunhofer diffraction occurs in the limit of small (<<1) Fresnel number, N_F.

Fresnel diffraction (near field diffraction) occurs as the distance of the source and the screen on which diffraction pattern is formed is kept at finite distance from the

diffracting object. For Fresnel diffraction the incident wave fronts on the obstacle are supposed to be spherical or cylindrical [41]. Fresnel diffraction occurs in the limit of large (>>1) Fresnel number.

The propagation of light wave with wavelength λ, passing through an aperture having a characteristic size a, over a distance L to screen is mathematically expressed by Fresnel number as follows:

$$N_F = \frac{a^2}{\lambda L} \tag{2.12}$$

Fresnel number is a dimensionless number.

2.5 Surface Enhanced Raman Scattering

Surface enhanced Raman scattering is defined as a surface sensitive technique that advances the small scattering cross section of conventional Raman scattering via introducing metal nanostructures to be excited by a monochromatic light source. The plasmonic properties of metal nanostructures serve for overcoming the weaknesses of conventional Raman scattering [42].

SERS process involves energy change of incident light through interaction of incoming radiation and the molecules adsorbed onto metal nanostructures. SERS is conventionally preferred for measuring agents having Raman signals that can be enhanced by nanostructures.

With the evolution of the SERS concept, reversed purpose innovative SERS applications that applications were investigated for detecting nanostructures whose presence can be detected by indicator molecules.

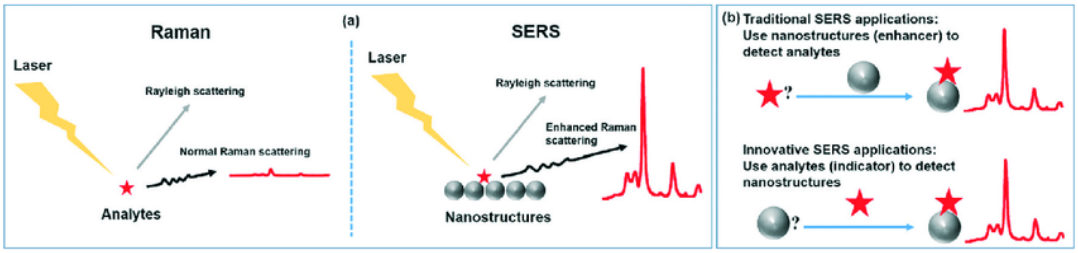

Figure 2.6 (a) Distinction between the Raman and the SERS techniques. (b) Innovative SERS applications [47].

Plasmons are defined as collective oscillation of electrons in conducting materials, on the surface of conducting materials and in the vicinity of conducting nanostructures.

Surface plasmons are collective excitation of conduction electrons at metal-dielectric interface. The excitation of surface plasmons is possible through prism coupling, grating coupling or with nanostructures that give rise to subwavelength corrugation [48], [49]. The strong interaction of surface plasmons with electromagnetic radiation form surface plasmon polaritons [50], [51]. In 1957, Ritchie introduced surface plasmon polaritons as electromagnetic excitations propagating along metal-dielectric interface having an exponential decay in the amplitude with increasing distance into each medium from the interface [52], [53]. Surface plasmon resonance corresponds to coherent oscillation of surface conduction electrons under the influence of electromagnetic radiation [50], [51]. In the case of surface plasmon resonance, photons are excited with certain angle of incidence and propagate parallel to the metal surface [55]. Materials holding negative real and narrow positive imaginary dielectric constants are capable of yielding surface plasmon resonances [54]. When the wavelength of the light source is kept constant and the metal surface is thin, the angle leading to surface plasmon resonance relies on the refractive index of the material in the vicinity of metal surface [56]. Typically, surface plasmon resonance frequency depends on the shape of the metal nanostructure and the dielectric function of the medium [57].

SPP oscillations travel along the metal surface in x and y-directions and they diminish in z-direction through the dielectric as illustrated in Figure 2.7.

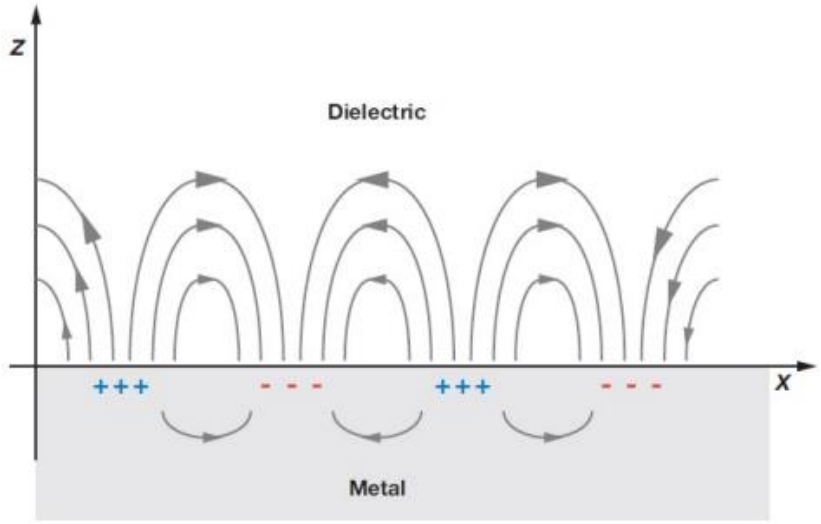

Figure 2.7 : Schematic representation of surface plasmon polariton (SPP) oscillations [54].

Surface plasmon condition indicates a classical model of two semi-infinite non-magnetic media with frequency- dependent dielectric functions ϵ_1 and ϵ_2 separated by a planar interface at z = 0. Unless the presence of an external source, the Maxwell's equations are stated as [59]:

$$\nabla \times \boldsymbol{H}_i = \epsilon_i \frac{1}{c}\frac{\partial \boldsymbol{E}_i}{\partial t} \tag{2.12}$$

$$\nabla \times \boldsymbol{E}_i = -\frac{1}{c}\frac{\partial}{\partial t}\boldsymbol{H}_i \tag{2.13}$$

$$\nabla.(\epsilon_i \boldsymbol{E}_i) = 0 \tag{2.14}$$

$$\nabla.\boldsymbol{H}_i = 0 \tag{2.15}$$

where *i* corresponds to the media and *i* = 1 at z < 0 and *i* = 2 at z > 0.

Solutions of the equations 2.12- 2.15 yields s-polarized and p-polarized electromagnetic modes. Assuming an ideal surface, a component of the electric field must be normal to the surface for the waves propagating along the interface. For that

reason, having electric field parallel to the interface negates s-polarized surface oscillations thus travelling waves having magnetic field parallel to the interface (p-polarized waves) are taken into consideration [59].

The x-axis is taken as the propagation direction to obtain the following equations:

$$\boldsymbol{E}_i = (E_{i_x}, 0, E_{i_z}) e^{-\kappa_i |z|} e^{i(q_i x - \omega t)} \tag{2.16}$$

$$\boldsymbol{H}_i = (0, E_{i_Y}, 0) e^{-\kappa_i |z|} e^{i(q_i x - \omega t)} \tag{2.17}$$

where q_i gives the magnitude of the wave vector that is parallel to the surface.

Solving Maxwell's equations for equations 2.16 and 2.17 the surface plasmon condition is expressed as:

$$q(\omega) = \frac{\omega}{c} \sqrt{\frac{\epsilon_1 \epsilon_2}{\epsilon_1 + \epsilon_2}} \tag{2.18}$$

where ϵ_1 and ϵ_2 are permittivity of metal and dielectric. The value of ω/c ratio, light wave vector, gives the magnitude of the incident field [59].

According to Drude semi-infinite metal in vacuum the magnitude of ϵ_2 is equal to 1 and ϵ_1 is formulated as:

$$\epsilon_1 = 1 - \frac{\omega_p^2}{\omega(\omega + \mathrm{i}\eta)} \tag{2.19}$$

where η is positive and infinitesimal. Plugging ϵ_1 into equation 2.18 yields the energy dispersion relation for the surface plasmon polariton as:

$$\omega^2(q) = \frac{\omega_p^2}{2} + c^2 q^2 - \sqrt{\frac{\omega_p^4}{4} + c^4 q^4} \tag{2.20}$$

where ω_p represents the corresponding plasma frequency. The surface plasmon polariton couples with free electromagnetic field when $q < \frac{\omega_s}{c}$ and yields nondispersive surface plasmon frequency when $q >> \frac{\omega_s}{c}$ given by:

$$\omega_s = \frac{\omega_p}{\sqrt{2}} \tag{2.21}$$

ω_s expresses the surface plasmon frequency [59].

2.5.1 Localized Surface Plasmon Resonances

Surface plasmons propagate freely as electron density waves along metal surfaces and take the form of localized electron oscillations on metal nanoparticles [58]. Unlike the propagating surface plasmons, localized surface plasmons are resonances in the vicinity of nanoparticles due to the interaction of incident electromagnetic field with the metal nanoparticle (MNP) that has a size narrower than the incident wavelength [54]. In other words, the confinement of non-propagating surface plasmon polaritons give rise to localized surface plasmon resonances via exciting MNP's by electromagnetic field at certain frequencies where the polarizability of the metal is expected to be significantly enhanced. Localized Surface Plasmon Resonances (LSPR) depend on dielectric function of the medium similar to surface plasmon resonance but the sensing volume of LSPR is confined in a restricted area compared to SPR. The collective oscillations of free electrons in the neighborhood of positively charged ions lead to the strong enhancement in the polarization of the metal surface as illustrated in Figure 2.8 [54].

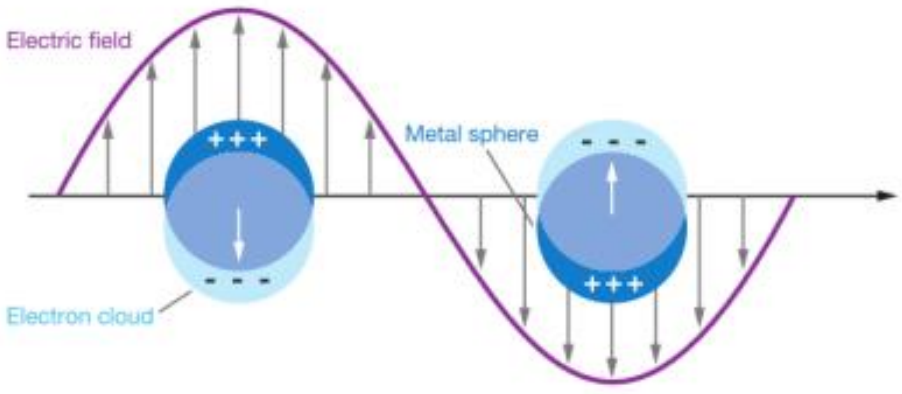

Figure 2.8 Schematic representation of localized surface plasmon resonance (LSPR) [54].

Conduction electrons oscillate coherently in the case of $R/\lambda < 0.1$ for a MNP resulting in formation of polarization charges on the surface. Turning to the dipole oscillations, the extinction cross section, σ_{ext}, is described by virtue of the Mie approach to Maxwell's equations [60]:

$$\sigma_{ext} = \frac{24\pi^2 R^3 \epsilon_m^{3/2} N}{\lambda ln(10)} \frac{\epsilon_i}{(\epsilon_r + \chi\epsilon_m)^2 + \epsilon_i^2} \quad (2.22)$$

where ϵ_m is the dielectric constant for the environment, ϵ_r and ϵ_i are real and imaginary parts of the metal dielectric function, R is the radius of the MNP, N is the electron density and χ is a constant affected by the shape of the particle [48].

The polarizability of a metal nanostructure is defined as the distortion of the electron due to the interaction with an incident electric field. The relation between the LSPR extinction peak with the dielectric environment is described in the following form [62]:

$$\alpha(\lambda) = 4\pi\epsilon_m(\lambda)R^3 \frac{\epsilon(\lambda) - \epsilon_m(\lambda)}{\epsilon(\lambda) + 2\epsilon_m(\lambda)} \quad (2.23)$$

where polarizability exhibiting a dipolar resonance as the denominator vanishes at $\epsilon_r = -2\epsilon_m$ is expressed. The peak LSPR frequency at the resonance condition is given by:

$$\omega_{LSPR} = \sqrt{\frac{\omega_p^2}{1 + 2\epsilon_m} - \gamma^2} \quad (2.24)$$

where ωp is the plasma frequency and γ is the damping rate of the bulk metal. LSPR peak wavelength manifests linear dependency on the refractive index for visible and near-infrared frequencies ($\gamma << \omega p$) [62].

The resonance is significantly affected by the variations in the geometry. Fundamentally, the resonance behavior of a metal nanowire subject to an x-polarized electromagnetic wave where the length to radius ratio $L/a > 1$ is formulated as:

$$\boldsymbol{E_1} = E_0 \frac{2\varepsilon_2}{\varepsilon_1 + \varepsilon_2} \boldsymbol{n_x} \quad (2.25)$$

$$\boldsymbol{E_2} = E_0\boldsymbol{n_x} + E_0\frac{\varepsilon_1-\varepsilon_2}{\varepsilon_1+\varepsilon_2}\frac{\alpha^2}{\rho^2}(1-2sin^2\varphi)\boldsymbol{n_x} + 2E_0\frac{\varepsilon_1-\varepsilon_2}{\varepsilon_1+\varepsilon_2}\frac{\alpha^2}{\rho^2}\sin\varphi\cos\varphi\,\boldsymbol{n_y} \quad (2.26)$$

where ε_1 and ε_2 are the complex dielectric constants of the wire and the medium [64].

Prevalent materials holding LSPR characteristics are noble metals including Au and Ag to be discussed in 2.5.3 [60].

2.5.2 Optical Properties of Noble Metals

To have a broader perspective about the optical properties of noble metals via interaction of metals and corresponding electromagnetic fields, macroscopic Maxwell equations or Maxwell equations in matter are to be introduced. The main idea is factoring bound charges and current out so the equations involve the free charges and currents [50].

$$\nabla.\boldsymbol{D} = \rho_{ext} \quad (2.27)$$

$$\nabla.\boldsymbol{B} = 0 \quad (2.28)$$

$$\nabla\times\mathbf{E} = -\frac{\partial\boldsymbol{B}}{\partial t} \quad (2.29)$$

$$\nabla\times\mathbf{H} = \boldsymbol{J}_{ext} + \frac{\partial\boldsymbol{D}}{\partial t} \quad (2.30)$$

where $\boldsymbol{D}$ represents dielectric displacement, $\boldsymbol{E}$ indicates electric field, $\boldsymbol{H}$ is magnetic field and $\boldsymbol{B}$ gives magnetic induction or magnetic flux density. Correlation with polarization $\boldsymbol{P}$ and magnetization $\boldsymbol{M}$ are expressed as:

$$\boldsymbol{D} = \varepsilon_0\boldsymbol{E} + \boldsymbol{P} \quad (2.31)$$

$$\boldsymbol{H} = \frac{1}{\mu_0}\boldsymbol{B} - \boldsymbol{M} \quad (2.32)$$

where ε_0 is the electric permittivity and μ_0 is the magnetic permeability of vacuum. When linear, isotropic and non-magnetic media conditions are being studied, the dielectric constant is dependent on frequency $\varepsilon = \varepsilon(\omega)$.

Specific properties of metals including Ag, Au and Cu varying from other dielectric materials are covered by the concepts of free electron plasma or solid plasma. Free-electron gas model describes the optical properties of metals characterized by the motion of free electrons in a fixed background consisting of positive ions neglecting the vibrations of ions. Free-electron gas model is applicable for noble metals at visible range of the spectrum [61].

The equation of motion for an electron of the plasma sea is formulated as:

$$m\ddot{\boldsymbol{x}} + m\gamma\dot{\boldsymbol{x}} = -e\boldsymbol{E} \tag{2.33}$$

where $\gamma = 1/\tau$ is characteristic collision frequency. The oscillation of the electron, $\boldsymbol{x}(t) = \boldsymbol{x}_0 e^{-iwt}$ where x_0 is a complex amplitude is rewritten as:

$$\boldsymbol{x}(t) = \frac{e}{m(w^2+i\gamma w)}\boldsymbol{E}(t) \tag{2.34}$$

For macroscopic polarization $\boldsymbol{P}$=-ne$\boldsymbol{x}$ the following expressions are formed:

$$\boldsymbol{P} = -\frac{ne^2}{m(w^2+i\gamma w)}\boldsymbol{E} \tag{2.35}$$

$$\boldsymbol{D} = \varepsilon_0\left(1 - \frac{ne^2}{m(w^2+i\gamma w)}\right)\boldsymbol{E} \tag{2.36}$$

Plasma frequency is then given by:

$$w_p^2 = \frac{ne^2}{\varepsilon_0 m} \tag{2.37}$$

The dielectric function of the free electron gas is expressed as:

$$\varepsilon(w) = 1 - \frac{w_p^2}{w^2+i\gamma w} \tag{2.38}$$

where the real part is given as:

$$Re\big(\varepsilon(w)\big) = 1 - \frac{w_p^2}{w^2+\gamma^2} \tag{2.39}$$

and imaginary part is given as:

$$Im(\varepsilon(w)) = \frac{w_p^2 \gamma}{w(w^2+\gamma^2)} \quad (2.40)$$

Metals holding negative $Re(\varepsilon(w))$ and negligible $Im(\varepsilon(w))$ are suitable for plasmonic studies [63].

2.6 Surface Enhanced Raman Spectroscopy

Surface-enhanced Raman spectroscopy is a supplement to Raman spectroscopy inserting metallic nanostructures to improve the intensity of the weak Raman scattering. SERS is useful to identify chemical composition of an unknown sample akin to Raman spectroscopy. Furthermore, the detection so identification from substantially smaller concentrations is feasible on account of signal amplification. The conventional Raman approach is based on the inelastic scattering produced by a laser irradiated analyte. Theoretically, analytes that are polarizable under laser irradiation are suitable for being detected by Raman spectroscopy but the weak Raman scattering signals hinder the detection of low concentrations of analytes. Further, fluorescence interference is an impediment to assessment of biological samples. In order to reduce fluorescence interference and enhance the detection sensitivity, SERS incorporates nanostructures commonly noble metal nanoparticles having suitable sizes, shapes and structures into established Raman technique and quench background fluorescence [46]. To have an elaborate description of the mechanism, the sample is placed on the nanostructured metal surface and illuminated by laser. The interaction of the metallic structure with incident light results in the excitation of plasmons. The excited plasmons concentrates the light at the neighborhood of the metal surface. Highly concentrated areas are defined as hot spots and enhance the Raman scattering emerging from the sample molecules. Thus, the Raman signal amplification enhances the limit of detection and enables the identification of significantly small concentration of substances.

In order to achieve the best detection and identification limits, the selection of the suitable excitation wavelength is critical. The excitation sources are lasers with

different wavelengths such as argon ion (488.0 and 514.5 nm), He:Ne (632.8 nm) and diode lasers (630 and 780 nm) leading to different SERS intensities so varying detection limits [47]. Effective data analysis of SERS spectra is correlated to the peak location, peak height and peak area.

2.6.1 SERS Substrates

The detection of adsorbed monolayers on metallic surfaces by Raman scattering is prominent to probe electrochemical processes where metallic electrodes and aqueous solutions are involved in various applications and demanding due to very small cross-section of the inelastic scattering. Under electrochemical control, various scientific researches carried out to achieving a Raman signature from adsorbed monolayers of metal surfaces during 1970's and only a few, including the detection of Hg_2Br_2, Hg_2Cl_2 and HgO in Hg electrode, succeed [67], [68]. In 1974, a roughened metal electrode surface is introduced by Fleischmann et al. intending to increase the number of adsorbed molecules yielding an enhancement in Raman intensity [3]. Jeanmaire et al. and Albrecht et al. independently identified a significant Raman intensity enhancement mechanism (calculated intensity enhancement ~10^5–10^6) enabling the observations of the spectra of molecules adsorbed on an electrode surface owing to the increase in the area caused by the roughening procedure [4], [5]. Later, Moskovits remarked the association of SERS intensities with enhanced fields emerging from localized surface plasmons in nanostructured metals [7] leading to a rapid growth in the interest and contribution of scientists to the field of study and improvement in the awareness of the effect that is named surface-enhanced Raman scattering (SERS).

A brief summary of related studies is covered above that are being discussed chronologically in more detail at the introduction part to reach the conclusion that roughened Ag electrodes are not the only choice of structures to be used as SERS substrates [67]. Investigation of Au and Cu nanoparticles are confirmed at the very

beginning of SERS studies paying attention to their ability to support excitation of surface-plasmons in the visible region [69].

SERS substrates can be manufactured by numerous methods producing nanostructures that can be randomly organized such as nanoparticles and nanoislands, highly ordered including gratings or betwixt these like nanowrinkles [70].

Key attributes of an ideal SERS substrate apart from strict performance requirements can be listed as uniformity, reproducibility, stability, ease of fabrication and cost-effectivity. Uniformity and reproducibility are essential features for quantitative assays, enhancement is vital for trace detection of chemicals allowing more sensitive and practical analysis. Moreover, the surface of the substrate should not suffer contamination due to the fabrication process. As a disadvantage, uniformity and reproducibility of a substrate are reduced as the enhancement gets higher so optimization of the fabrication processes is necessary [70], [71].

2.6.1.1 Substrates for Direct (Label Free) Detection

Direct protocols endorse the identification of compounds through their own Raman spectrum and are applicable for large cross-sections including explosives [72], contaminants such as pesticides and food dyes [70], [73]. Figure 2.9 illustrates the direct protocol and indirect protocol to be discussed in 2.6.1.2.

A SERS tag is functionalized with antibodies, selectively binds to the analyte that is adsorbed on the nanoparticle and detected through its Raman spectrum. Detection is achieved through the spectrum of the Raman reporter included in the SERS tag [70].

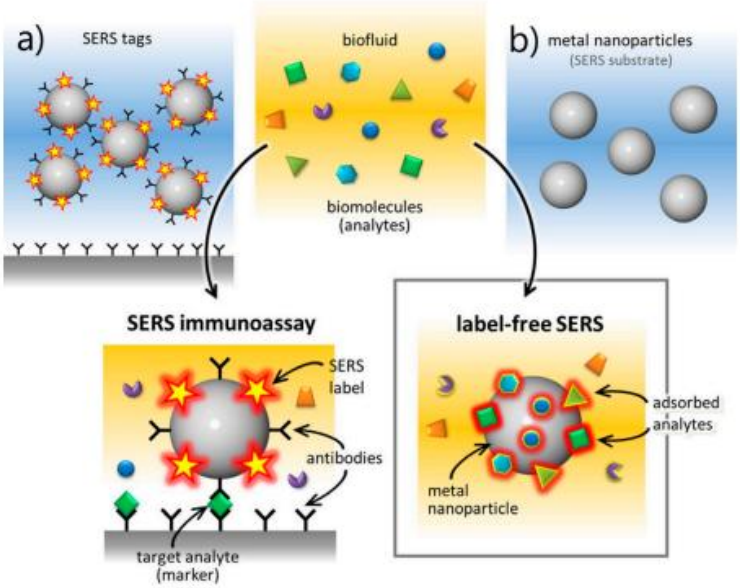

Figure 2.9 (a) Indirect protocol. (b) Direct protocol [74].

Corresponding fabrication methods for unstructured nanoparticles (aggregated NPs in solution) can be classified as wet chemistry and laser ablation for NP synthesis, molecular linkers and laser tweezers as aggregating method. Corresponding fabrication methods for structured nanoparticles (NPs assembled on a surface) can be listed as electrochemical roughening/deposition, deposition on functionalized surfaces, ink-jet printing, screen printing, pen on paper, electrospinning and laser direct writing. Corresponding fabrication methods for structured surfaces (ordered array of NP's) can be introduced as anodic alumina template, electron beam lithography, interference lithography and soft lithography [70].

Efrima et al. introduced Ag nanocolloids on bacterial cells making use of silver nanoparticles produced inside and on the outer wall of the Escherichia coli bacteria. On the outer walls enhanced signal is received demonstrating the amplification of the Raman signal relative to proteins, peptides, amino acids, molecules, and functional groups existing in the affinity of the nanocolloids [82].

Xu et al. performed a laser writing method to produce a SERS active silver pattern in a microfluidic circuit, starting from a solution containing $AgNO_3$, trisodium citrate, and ammonia as show in Figure 2.10 [83].

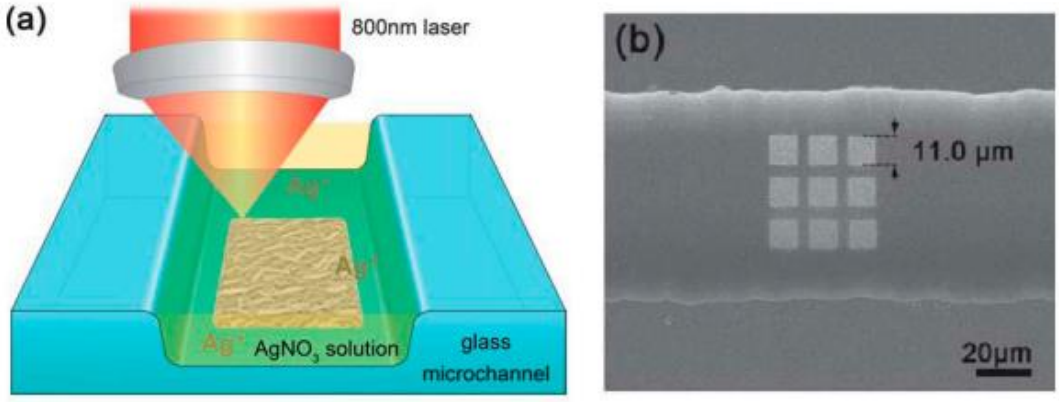

Figure 2.10 (a) Laser writing method used to fabricate SERS substrates. (b) SEM image of the SERS substrates patterned into a microfluidic circuit [83].

The most significant feature of this method is creating SERS active microstructures of the desired shape.

Shanmukh et al. investigated respiratory human viruses in real-time by introducing silver nanorod arrays as a choice of plasmonic substrates that are fabricated via the oblique angle deposition method. SERS spectra were obtained from considerably small volumes of samples [80].

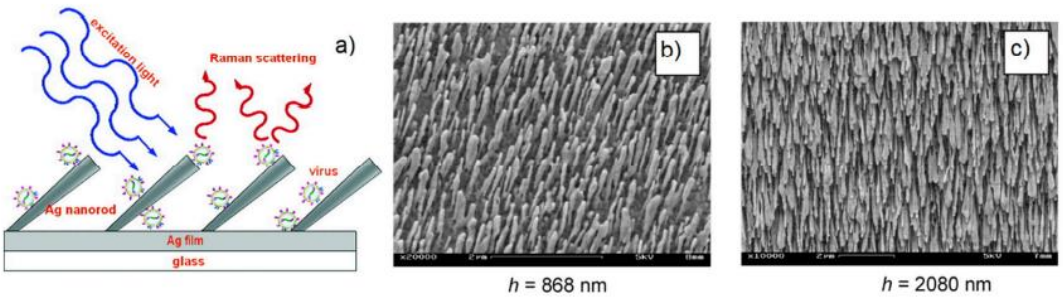

Figure 2.11 a) Scheme of silver nanorod array substrates b) SEM image of nanorod array h=868 nm c) SEM image of nanorod array h=2080 nm [80].

Xu at al. investigated proteins by retaining them in the native state. Iodine-modified silver colloids are used to avoid the denaturation providing a good reproducibility and sensitivity of the SERS signal. The SERS spectra of hen egg white lysozyme, avidin, cytochrome c, hemoglobin, and BSA obtained as illustrated in Figure 2.12 [81].

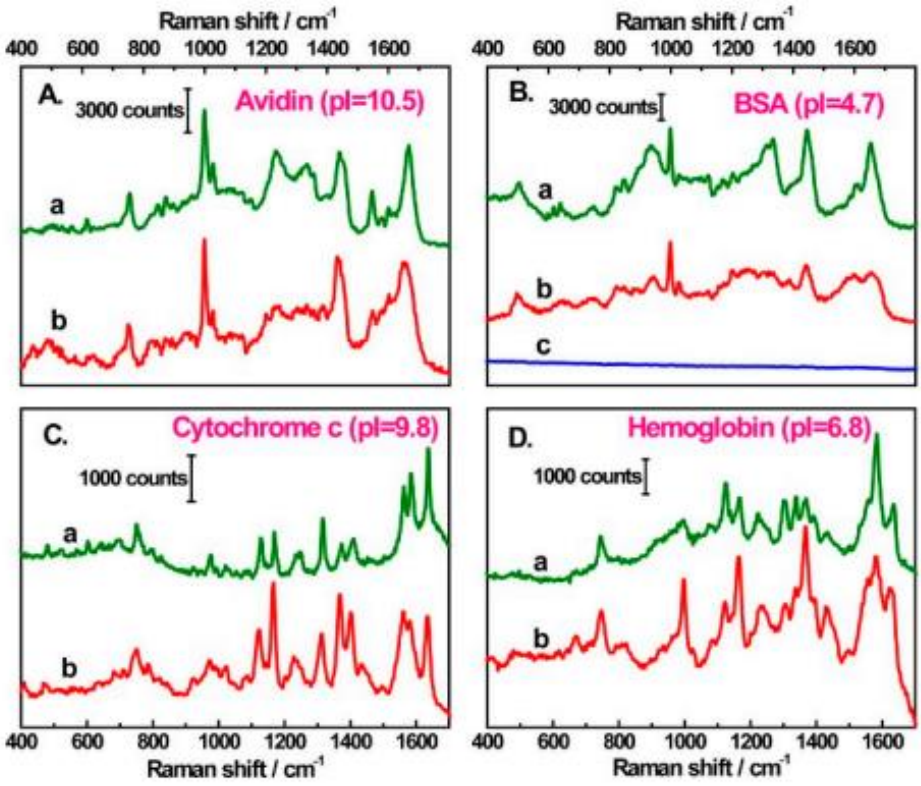

Figure 2.12 Comparison of the normal Raman (green line) and amplified SERS spectra (red line) of Avidin (A), BSA (B), Cytochromo c (C), and Hemoglobin (D) [81].

SERS spectra are recorded with the iodide-modified Ag nanoparticles method. Sample concentrations are set as 300, 300, 3, 30 μg/mL. The blue line c represents the aggregation effect. No Raman signal is detected before aggregation [81].

2.6.1.2 Substrates for Indirect Detection

Indirect protocols make use of molecular recognition elements reducing the spectral interference from the sample matrix [76].

SERS labels are defined as complex species including an efficient Raman reporter and designed to selectively bind to the desired molecule where the analyte is detected through the spectrum of the Raman reporter [70].

SERS labels consist of a plasmonic core, a Raman reporter, and a protective shell as shown in Figure 2.13.

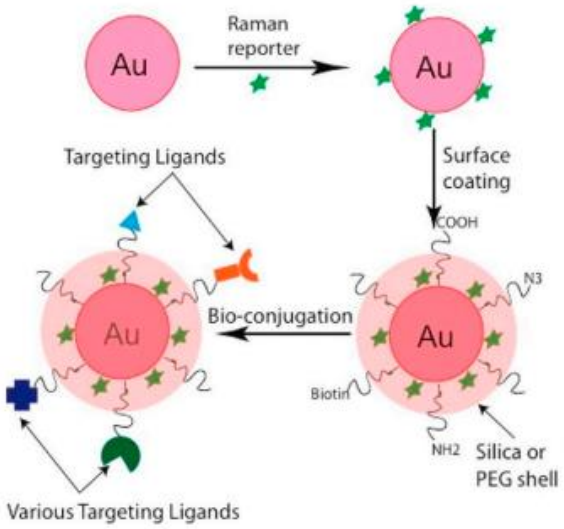

Figure 2.13 Configuration of a SERS tag [75].

The plasmonic core should be designed to optimize the enhancement in the target spectral region by using nanoparticles with different geometries such as nanospheres, by aggregating nanoparticles to form dimers or trimers [77] or by manufacturing more complex structures yielding higher density of hot spots [70].

The Raman reporter should be photochemically stable and have a large cross-section like rhodamines, the crystal violet cation [75] and strongly bind to the surface of the nanoparticles as small organic molecules [78]. Utilizing the resonance Raman effect

is viable by making use of these dyes. The Raman reporter is required to have bands in a clean spectral region. The possibility of overheating must be prevented while enhancing the Raman signal [75].

A protective Shell such as polyethylene glycole (PEG) is used to avoid the aggregation of nanoparticles in unintended zones, to avert the detachment of the reporter from the surface and to detain non-specific adsorption of cellular components [76].

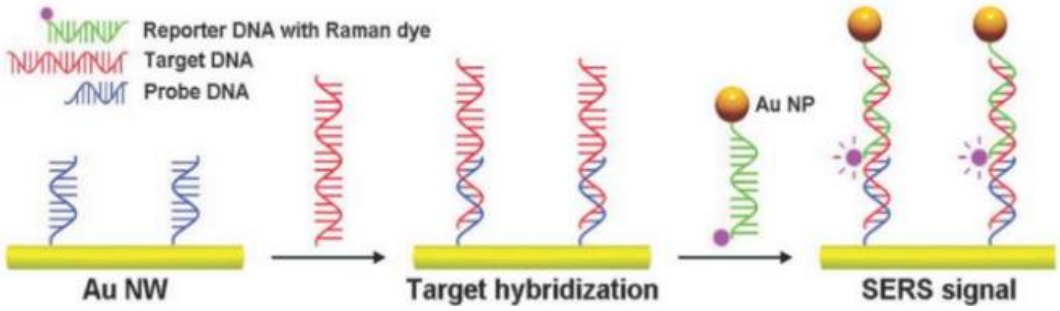

Figure 2.14 An indirect SERS application for DNA detection [79].

Kang et al. studied Au particle-on-wire system to be used as a specific and sensitive sensor for multiplex sensing of target DNAs. An indirect surface-enhanced Raman spectroscopy (SERS) application is used for PCR-amplified pathogenic DNA detection as illustrated above in Figure 2.14 [79].

2.7 Enhancement

SERS enhancement is proportional to the increase in the cross-sectional area of the molecules [65].

Lombardi and Birke grounds overall SERS enhancement on three resonance denominators incorporating the surface plasmon resonance, the metal-to-molecule charge transfer resonance and the molecular resonance [66].

Electromagnetic enhancement arises from the excitation of LSPR by an incident laser giving rise to large electromagnetic fields at the NP surface. The metal-to

molecule charge-transfer resonance takes place when analytes are adsorbed onto the roughened surface of NPs where the excitation frequency is in resonance with adsorbate's charge transfer transition. This mechanism is conventionally defined as chemical enhancement. Molecular resonance prevails as the excitation source coincides with the electronic transition of chromophore groups if present in the analyte [66].

Depending on parameters including the characteristics of nanomaterials, interparticle distance, excitation wavelength and molecular recognition elements, the contribution of each resonance on Raman enhancement varies.

2.7.1 Electromagnetic-Field Enhancement

At the surface of the substrate the localization of light yields electromagnetic-field enhancement that is the strongest contribution to the SERS enhancement possessing two distinct contributions, namely the local field (or near field) enhancement and the re-radiation enhancement. The Raman and SERS scattered Powers are related as follows [70]:

$$P_{SERS} = G_{SERS} P_{Raman} \tag{2.41}$$

where G_{SERS} is (total) SERS enhancement factor given by [70]:

$$G_{SERS} = G_{SERS}^{Em} G_{SERS}^{Chem} \tag{2.42}$$

In order to estimate the average G_{SERS} , the following relation is used [87]:

$$G_{SERS} = \frac{P_{SERS}}{P_{Raman}} \frac{N_{SERS}}{N_{Raman}} \tag{2.43}$$

N_{Raman} and N_{SERS} are the number of molecules irradiated by the laser in the actual Raman and in the SERS experiment.

2.7.1.1 Local Field Enhancement

The excitation of surface plasmons leads to a strong spatial localization so amplification of the incident laser light in small spatial regions defined as hot spots that are identified as very sharp tips or as nanogaps between nanoparticles [70], [86]. The electromagnetic field experienced by the molecules in hot spots is stronger than the field they would experience in the absence of the metallic substrate [86].

The external electric field oscillating at the laser frequency, ω_L, induces a dipole $p(\omega_R)$ expressed as [70]:

$$\boldsymbol{p}(\omega_R) = \hat{\alpha}_R(\omega_R, \omega_L)\boldsymbol{E}(\omega_L) \tag{2.44}$$

where ω_R repreents the Raman (angular) frequency and $\hat{\alpha}_R(\omega_R, \omega_L)$ is s the Raman polarizability tensor of the molecule.

The radiated power, P_{Raman}, is defined as [61]:

$$P_{Raman} = \frac{\omega_R^4}{12\pi\varepsilon_0 c^3}|\boldsymbol{p}(\omega_R)|^2 = \frac{\omega_R^4}{12\pi\varepsilon_0 c^3}|\hat{\alpha}_R(\omega_R, \omega_L)\boldsymbol{E}(\omega_L)|^2 \tag{2.45}$$

where $\varepsilon_0$is the dielectric constant in vacuum and c is the speed of light in vacuum. To express in [photons/s] [61]:

$$P_{Raman}[W] = \hbar\omega\, P_{Raman}\ [photons/s] \tag{2.46}$$

When a metallic substrate is present in the vicinity of the molecule, molecule experiences the local electric field stronger than the incident field. The local field enhancement is given by [61], [85], [70]:

$$M_{Loc}^{Z}(\omega_L) = \frac{|\boldsymbol{E}_{Loc}(\omega_L)|^2}{|\boldsymbol{E}(\omega_L)|^2} \tag{2.47}$$

where Z specifies the linear polarization of incident laser along the z-axis, perpendicular to the propagation direction.

2.7.1.2 Re-Radiation Enhancement

For a dipole in the vacuum, the radiated power diffuses into the space supporting the conventional emission pattern of a dipole. In the presence of interfaces, the electromagnetic field irradiated by the dipole is scattered at these interfaces and is back scattered at the dipole position prompting environment-dependence of the dipole by influencing the way in which the dipole radiates power. Re-radiation enhancement is formulated as [70]:

$$M_{Rad} = 1 + \frac{6\pi\varepsilon_0}{|\boldsymbol{p}_0|^2}\frac{1}{k^3} Im\{\boldsymbol{p}_0^*.\boldsymbol{E}_{SR-0}\} \quad (2.48)$$

where $\boldsymbol{p_0}$ is the complex amplitude of the dipole, $\boldsymbol{E}_{SR-0}$ is the self-reaction field (in vacuum = 0), and *k* is the wavevector of the emitted radiation.

2.7.2 Chemical Field Enhancement

Chemical Field Enhancement is vital as it directs the spectral pattern of the SERS spectra consisting of the Raman shifts and the band intensity ratios. Interaction of the metallic structure and the analyte molecule that is in the neighborhood of it leads to a change in the Raman polarizability tensor [61]. Non-resonant chemical effect and resonant charge transfer chemical effect can contribute to the chemical enhancement mechanism [88].

The chemical enhancement can be formulated as [89]:

$$G_{SERS}^{Chem} = \frac{\sigma_k^{ads}}{\sigma_k^{free}} \quad (2.49)$$

σ_k^{ads} and σ_k^{free} are the Raman cross-sections of the k-th vibrational mode of the adsorbed and of the free molecule.

2.7.2.1 Non-resonant Chemical Effect

For non-resonant chemical effect, the interaction of the molecule and the metal does not influence a new electronic state but lead to a significant variation in the geometry and electronic structure of the molecule yielding a moderate modification of the Raman shifts and of the intensity of the vibrational modes [70].

2.7.2.2 Resonant Charge Transfer Chemical Effect

The interaction between the molecule and the metal leads to the initiation of a metal–molecule charge transfer state. In the case of excitation by a laser source in resonance or pre-resonance with this state, Raman modes are remarkably enhanced and coupled to the allowed electronic transitions [70], [94].

2.7.3 Enhancement Factor

Enhancement factor (EF) arise from the contributions of the chemical and the electromagnetic enhancement subject to the geometry of the nanostructures, gaps between aggregated nanostructures, polarization and LSPR wavelength [90].

The electromagnetic enhancement factor (EF) is given by [91]:

$$EF(r_m, \omega) = \left|\frac{E(r_m,\omega)}{E_{inc}(\omega)}\right|^4 \tag{2.50}$$

where $E_{inc}(\omega)$ represents the incident field, r_m is the position of the molecule. Formula 2.50 does not include the chemical contributions mentioned in 2.7.2.

E. C. Le Ru et al. discussed different definitions for SERS enhancement factor by focusing on three main aspects. First concern is including non-SERS properties of probes in the definition. Second crucial point is identifying the dependence to experimental conditions including the SERS probe and the dependence to intrinsic parameters of SERS substrate contributing to the performance. Lastly, depending on

the application identifying the distinction between average SERS EFs and MF-SERS EFs is important. A general definition of EF can be deduced by making use of various applications of SERS such as single molecule, multiple molecules, spatial distribution and orientations of the probe on the surface. EF is an important number in the investigation and characterization of the SERS effect. E. C. Le Ru et al. classified the applicable EF calculation methods as the single molecule EF, the analytical chemistry point of view and the SERS substrate point of view [92].

2.7.3.1 Single Molecule Enhancement Factor

SERS enhancement experienced by a molecule at a distinct point is defined as single molecule EF. Single molecule EF depends on the geometry and orientation of the substrate and the position and orientation of the probe.

Single molecule enhancement factor is formulated as:

$$SMEF = \frac{I_{SERS}^{SM}}{\langle I_{RS}^{SM} \rangle} \tag{2.51}$$

where I_{SERS}^{SM} and $\langle I_{RS}^{SM} \rangle$ are single molecule SERS intensity and the average Raman intensity per molecule, respectively. Maximum SMEF on a SERS substrate is important as SM signals are recorded from the points of highest enhancement, hot spots [92].

2.7.3.2 Analytical Chemistry Point of View

Under non-SERS conditions, an analyte solution having a concentration, c_{RS} , producing a Raman signal, I_{RS}; under SERS conditions the same analyte on a SERS substrate having different concentrations, c_{SERS}, giving a SERS signal, I_{SERS}, can be investigated to study the analytical enhancement factor (AEF) given below:

$$AEF = \frac{I_{SERS}/c_{SERS}}{I_{RS}/c_{RS}} \tag{2.52}$$

Adsorption properties, surface coverage of the probe and sample preparation procedures are related parameters affecting analytical enhancement factor that is useful for SERS active liquids including colloidal solutions [92].

2.7.3.3 SERS Substrate Point of View

The comparison of average SERS enhancements across different substrates is possible by defining substrate enhancement factor (SSEFs) investigating the distribution of the SMEF on the substrate. The commonly used definition for average SERS EF is formulated as:

$$EF = \frac{I_{SERS}/N_{Surf}}{I_{RS}/N_{Vol}} \tag{2.53}$$

where I_{SERS} and I_{RS} are SERS and Raman intensities, N_{Vol} is the average number of molecules in the scattering volume for Raman measurement and N_{Surf} is the average number of adsorbed molecules in the scattering volume for SERS applications [92].

$$N_{Vol} = c_{RS}V \tag{2.54}$$

where V represents the scattering volume for non-SERS measurements [93].

CHAPTER 3

FINITE-DIFFERENCE TIME-DOMAIN (FDTD) METHOD

3.1 The FDTD Method

The Finite-Difference Time-Domain (FDTD) method is a solver of Maxwell's equations in complex geometries providing direct time and space solution of the problem in the fields of electromagnetics and photonics [95]. Moreover, FDTD offers the frequency-solution by making use of Fourier transforms yielding the calculations such as transmission and reflection of light [96]. The basic workflow of the FDTD simulations is given by Table 3. 1.

Table 3. 1 Basic workflow of FDTD Simulations

Module	Process Steps
FDTD Designer	Build object (Layout)
	Define required parameters
	Assign input field
FDTD Simulator	Initiate simulation
	Update E-field
	DFT analysis
	Time step
FDTD Analyser	Post Data Analysis

3.1.1 Simulation Key Parameters and Skills

In the simulation step, care must be taken while defining the objects, mesh structure, boundary conditions, material parameters, structures, sources, attributes, and monitors. The structure encompasses the modelling of the geometry of the system

while mesh structure is finite regions of the structure that interacts with the EM fields. Boundary conditions are set at the ends of the introduced structure to limit the solid material in a realistic manner, so that EM waves and scattered waves are bound to the simulation area. The type and the size of the material and its response to the E-field with respect to the material's refractive index and dielectric function are the effective simulation parameters. Sources are defined as the EM wave suppliers including dipoles, plane waves, Total-Field Scattered-Fields (TFSF), and Gaussian. Attributes are useful for dynamic systems, such as rotating bodies. Lastly, the monitors are the predefined outputs of the simulation.

Some key design rules to adhere to are as follows. The mesh size must be set to minimum of one tenth of the incident wavelength. The mesh accuracy can be enhanced by using mesh settings. Extra meshes can be defined to the area of interest if necessary. Simulation bandwidths can be set. The amplitudes of the sources can be edited in the case of stronger power source requirements. The phase of the incident light can be adjusted to the simulation needs. Time-domain can be set by changing the pulse length, and as the pulse length increases the time-domain decreases accordingly. The k-vector can be adjusted.

3.1.2 Physics Behind the Solver

The basis of the FDTD lies under Yee algorithm that is proposed in 1966 introducing a set of finite-difference equations for the time-dependent Maxwell's curl equation [98]. Yee algorithm solves for both electric and magnetic fields in time and space making use of the coupled Maxwell's curl equations rather than solving them explicitly. Yee algorithm centers the $\vec{E}$ and $\vec{H}$ components in three-dimensional space and also in time. Yee space lattice with the electric and magnetic field vector component is shown in Figure 3. 1 [99].

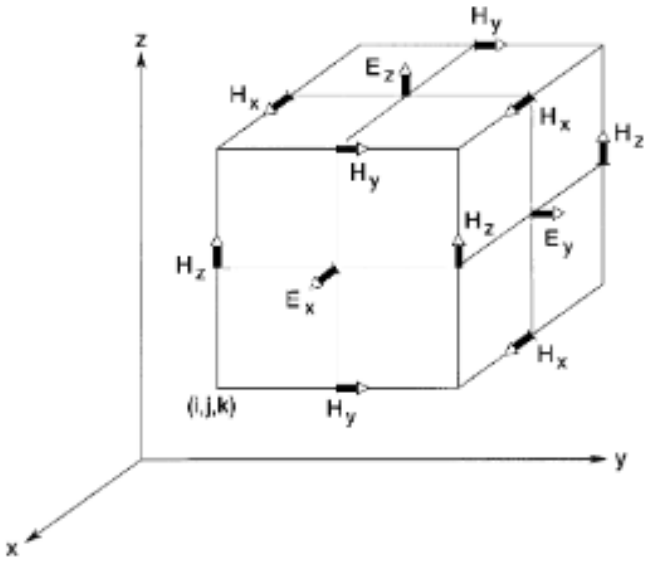

Figure 3. 1 Yee space lattice with the electric and magnetic field vector component [99].

3.2 Simulation Model Details

The simulations consist of double-nanowire CAD models that are imported. The nanowire is modelled as a pentagonal wire that is coated by TiO_2. The edges of pentagonal wire are rounded by giving radius of curvature.

The pentagonal geometry is the preferred due to the information provided by previous works stating that the corners yield considerably large EF defined as lightning rod effect that may lead to nanoparticles acting like antennas [101]. 2 nm radius of curvature is given in order to obtain the structure closest to the actual geometry.

In literature, the SERS enhancement for silver is observed for excitation wavelengths varying from 600 nm to 1200 nm [100]. Silver is observed to yield highest EF's by virtue of its absorption properties. Alignments in the particle shape may lead to broadening of LSPR range and also tuning of nanoparticles to certain LSPR peaks so improving EF accordingly is possible. Most widely used Raman wavelength

offering optimal performance including scattering efficiency is 785 nm. 532 nm is a significant wavelength that is preferable especially for temperature sensitive samples such as carbon nanotubes in order to prevent heat damage. 1064 nm wavelength choice is useful for reducing fluorescence. In order to avoid the UV destruction on the sample near-IR lasers (660 nm belongs to that range) are being used for eliminating fluorescence. The wavelengths of interest for the FDTD analysis in the scope of the thesis are 532nm, 660 nm and 785 nm.

Simulation Model Details are given by Table 3. 2.

Table 3. 2 Simulation Model Details

Material of Wire	Silver
Scale	Nano
Material of Coating	TiO_2
Geometry of the Model	Pentagonal
Radius of Curvature	2 nm
Thickness of TiO_2	2,4,6 nm
Lengtgh of Wire	500 nm
Diameter of Wire	50 nm
Source	Planar Source
Wavelength	532 nm 660 nm 785 nm
Polarization Angle	0,30,45,60,90
Orientations of the wires	Double Wire- Parallel orientation Double Wire- with 90 degrees crossing in the centre

3.3 Experimental Background and Correlation with the FDTD Analysis

3.3.1 AgNW Synthesis and Foil Fabrication

Silver nanowires are synthesized through polyol method that is widely used to produce metallic nanoparticles. The polyol method consists of suspending the metal precursor in a glycol solvent. The solution is heated to a certain temperature that is defined as refluxing temperature critical for preventing the liquid loss due to relatively weak boiling point of organic substances.

The conventional polyol process is adjusted to be convenient for extensive scale AgNW synthesis. 0.45 M, 80 ml EG ethylene glycol (EG) solution of PVP and 10 mg sodium chloride (NaCl) (99.5%) to be dissolved in EG at 100℃ is prepared. After heating up to 100℃, the solution is refrigerated to room temperature. Concurrently, 0.12 M silver nitrate (AgNO3) (99.5%) solution in 40 ml EG is prepared at room temperature. Subsequently, the solution is heated to 120°C in a silicon oil bath and the PVP/EG solution is poured into AgNO3 /EG solution in 10 minutes interval. The oil bath is set to 160°C and after reaching the 160℃ the solution is annealed 90 minutes further. A magnetic stirrer of 1000 rpm is used along the process. Centrifuge process is utilized to maintain the purification of AgNWs that is removing PVP and EG. Acetone is used to dilute the solution and the solution is centrifuged at 8000 rpm for 20 minutes twice and following that the nanowires are dispersed in ethanol and centrifuged at 8000 rpm for 20 minutes one more time. The yielding product is dispersed in deionized water ready for the fabrication of foils. [102]. Vacuum filtration of the measured amount of colloidal AgNWs through teflon based hydrophilic 47 mm filter papers having 3 μm pore size and peeling from the filter results in a 40 mm width AgNW based foils [103]. The process and end-product are shown in.

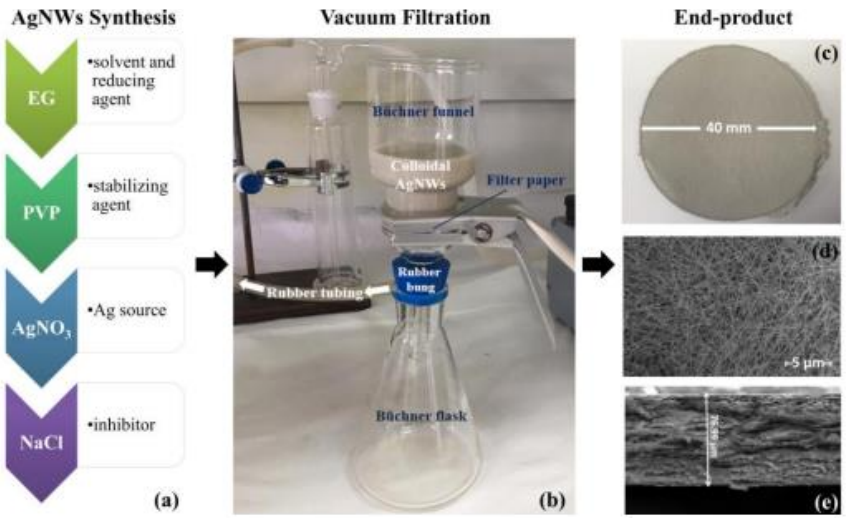

Figure 3. 2 a) Ingredients for the synthesis of AgNWs, b) Vacuum filtration setup, c) AgNW foils, d) top-view, and e) cross-sectional SEM images of AgNWs foils [103].

3.3.2 TiO_2 Coating using ALD

TiO_2 is deposited at various thicknesses by ALD on AgNW foils. The coating is used as a tunneling barrier against quantum tunneling effects, optimizes the detection and even promoting EF is possible.

TiO_2 thin films were deposited on AgNW foils using a plasma enhanced ALD (PEALD) system (SENTECH SI ALD LL). Tetrakis (dimethylamido)titanium (TDMAT) (Sigma-Aldrich) and O_2 plasma were used as titanium precursor and co-reactant, respectively. Nitrogen (N_2) of 5N purity was used as the carrier and purge gas at flow rate of 40 sccm. The working pressure was 0.2 mbar. The plasma source is an RF generator with a frequency of 13.56 MHz TiO_2 thin films were deposited for 2, 5, 10, 20, and 50 ALD cycles on different AgNW foil substrates resulting in different film thicknesses. The substrate was heated to 150°C for all depositions.

3.3.3 Correlation with the FDTD Analysis

3-dimensional network of AgNWs having nanogaps in-between bring about high-density SERS hot spots. The complex network has numerous orientations of nanowires with respect to each other. By taking subsystems from that complex structure and analyzing their behavior in the scope of SERS enhancement contributes to the experimental studies that has been carried by defining the optimum parametric set to be studied further.

The CAD models representing parallel oriented and cross oriented AgNWs are illustrated in Figure 3. 3.

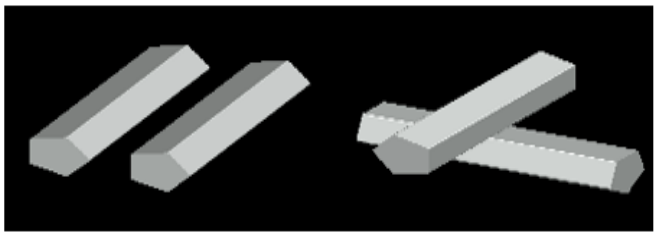

Figure 3. 3 CAD Models of parallel oriented and cross oriented AgNWs

Black and white version of the SEM image of the Ag NW networks and the mask image of the Ag NW networks are provided in Figure 3. 4 showing the complex network of Ag NW's and their orientation with respect to each other.

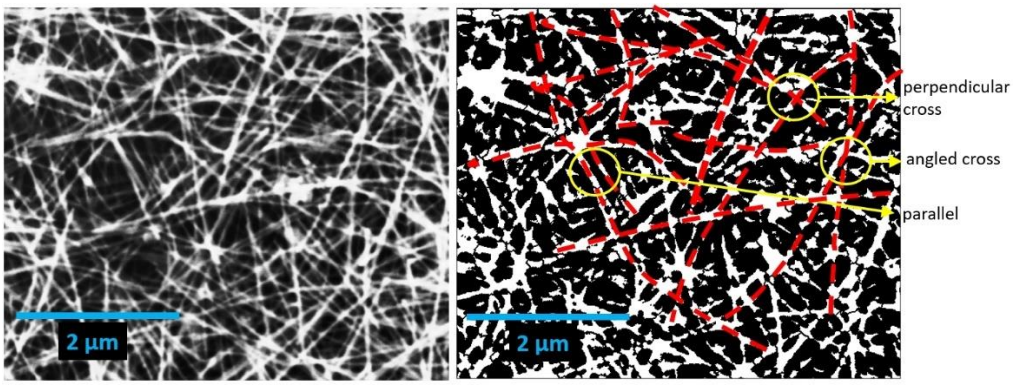

Figure 3. 4 SEM image of the Ag NW networks and the mask image of the Ag NW networks

Perpendicular cross, angular cross and parallel orientations are shown by circular marks. Current simulation tools are not eligible and computers also in terms of memory to analyze all the network at once so subsystems considering these different orientations are taken to be analyzed.

CHAPTER 4

RESULTS AND DISCUSSION

4.1 Effect of Distance

4.1.1 Parallel Orientation Model

The details of the simulation model including two parallel oriented TiO_2 coated AgNWs are given by Table 4. 1.

Table 4. 1 Parallel Model Details (PA= 0^o)

Property	Magnitude (nm)
Radius of Curvature	2
Length of Nanowire	500
Radius	50
Center Wavelength	532
Wavelength Span	100
Distance Btw Wires	5,10,15
TiO_2 Thickness	2

FDTD analysis results yielding the regarding EFs are given by Table 4. 2.

Table 4. 2 Resulting EFs Depending on Distance

Distance Btw Wires (nm)	EF (PA=0^o)
5	7.07E+05
10	1.30E+05
15	6.55E+04

Analysis concerning 5 nm, 10 nm and 15 nm distances yield that the related EF values for 5 nm distance gives optimum results.

To have an accurate conclusion analyzing the distance values around 5 nm is significant so new runs for 2 nm, 3 nm, 4 nm and 6 nm distances were investigated for parallel oriented TiO_2 coated AgNWs with 532 nm source wavelength and PA=0^o.

The FDTD analysis results yielding the regarding EFs for the samples are given by Table 4. 3.

Table 4. 3 Resulting EFs for Parallel Oriented TiO_2 Coated Samples Depending on Additional Distance Values (λ=532 nm)

Distance Btw Wires (nm)	**EF (λ=532 nm)**
2	2.34E+05
3	7.07E+05
4	9.23E+05
6	1.30E+05

Distance versus EF graph of parallel oriented TiO_2 coated AgNWs is shown in Figure 4. 1.

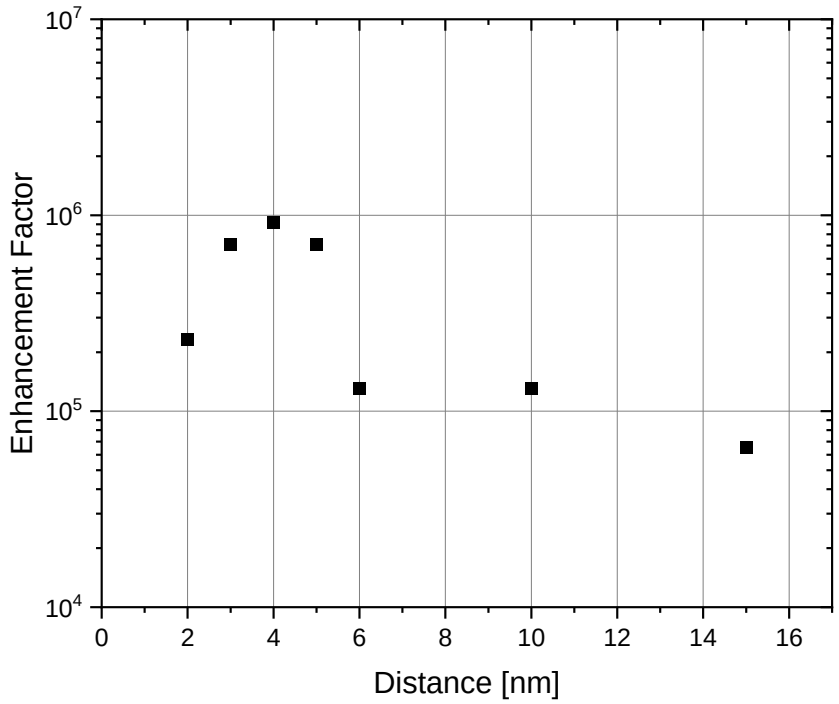

Figure 4. 1 Distance vs EF Graph of Parallel Oriented TiO_2 coated AgNWs (PA=0º)

4.1.2 Cross Shape Orientation Model

The details of the simulation model including two cross oriented uncoated AgNWs are given by Table 4. 4.

Table 4. 4 Cross Shape Model Details (PA=90º)

Property	**Magnitude (nm)**
Radius of Curvature	2
Length of Nanowire	500
Radius	50
Center Wavelength	532, 660, 785
Wavelength Span	100
Distance Btw Wires	2,3,4,5,6,7,10,15

FDTD analysis results yielding the regarding EFs are given by Table 4. 5.

Table 4. 5 Resulting EFs Depending on Distance (λ=532, 660 and 785 nm)

Distance Btw Wires (nm)	**EF (λ=532 nm)**	**EF (λ=660 nm)**	**EF (λ=785 nm)**
5	9.24E+05	6.25E+06	2.86E+04
10	2.34E+05	1.46E+04	1.30E+03
15	2.34E+05	1.46E+04	2.40E+03

After performing analysis for 5 nm, 10 nm and 15 nm distances, the related EF values indicated that 5 nm distance gives best results. To have an accurate conclusion analysing the distance values around 5 nm is significant so new runs for 2 nm, 3 nm, 4 nm, 6 nm and 7 nm distances were investigated with 660 nm source wavelength and and PA=90^{o} for both uncoated and 2 nm TiO_2 coated samples. The FDTD analysis results yielding the regarding EFs for uncoated samples are given by Table 4. 6.

Table 4. 6 Resulting EFs for Uncoated Samples Depending on Additional Distance Values (λ=660 nm)

Distance Btw Wires (nm)	**EF (λ=660 nm)**
2	3.16E+07
3	2.69E+07
4	2.40E+07
6	5.31E+06
7	3.42E+06

Distance versus EF graph of uncoated AgNW's is shown in Figure 4. 2.

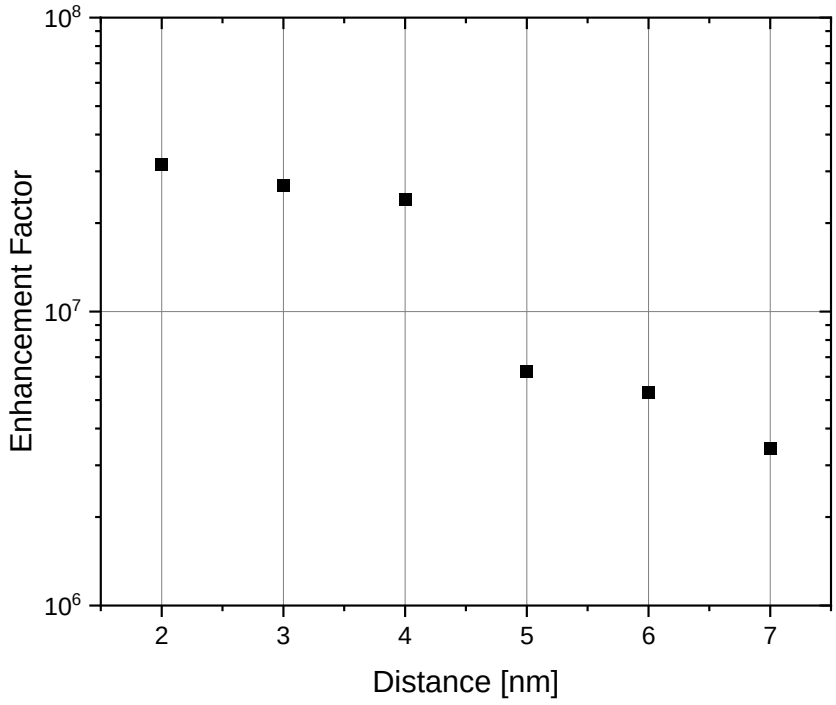

Figure 4. 2 Distance vs EF Graph of Uncoated AgNWs (PA=90°)

The details of the simulation model including two cross oriented TiO_2 coated AgNWs are given by Table 4. 7.

Table 4. 7 Cross Shape Model Details (TiO_2 Coated)

Distance Btw Wires (nm)	**EF (λ=532 nm)**	**EF (λ=660 nm)**	**EF (λ=785 nm)**
5	9.24E+05	1.87E+06	6.55E+04
10	3.91E+05	6.56E+04	2.86E+04
15	6.55E+04	2.40E+03	6.55E+04

The analysis of 2 nm TiO_2 coated samples for additional 2 nm, 3 nm, 4 nm, 6 nm and 7 nm distances were investigated with 660 nm source and PA=90°. The FDTD analysis results yielding the regarding EFs for uncoated samples are given by Table 4. 8.

Table 4. 8 Resulting EFs for TiO_2 Coated Samples Depending on Additional Distance Values (λ=660 nm)

Distance Btw Wires (nm)	**EF (λ=660 nm)**
2	7.07E+05
3	2.40E+07
4	1.30E+07
6	2.34E+05
7	2.34E+05

Distance versus EF graph of TiO_2 coated AgNWs is shown in Figure 4. 3.

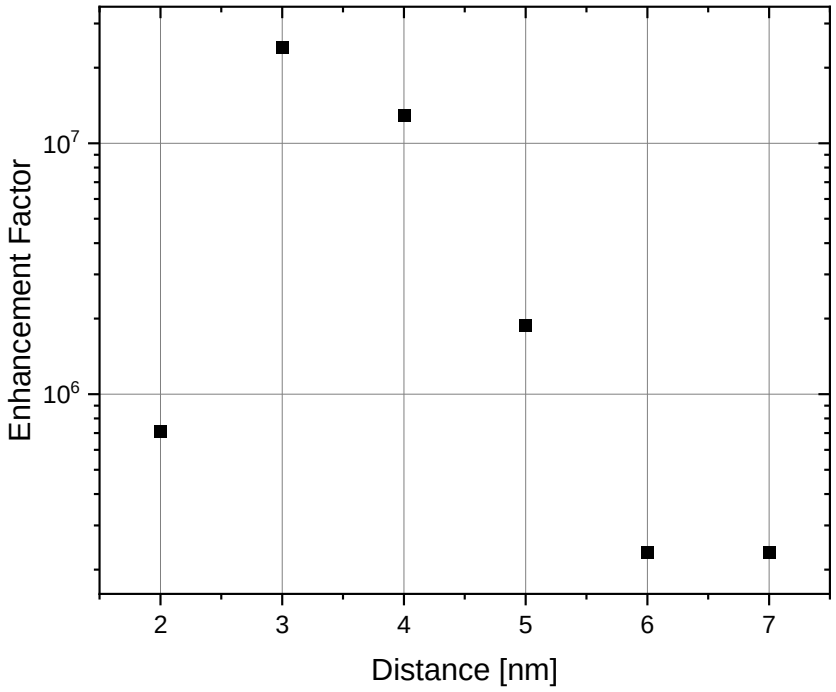

Figure 4. 3 Distance vs EF Graph of TiO_2 Coated AgNWs (PA=90º)

FDTD simulation sets to analyse the effect of distance yield that the optimum distance for uncoated cross oriented AgNWs is 2 nm and for TiO_2 Coated cross oriented AgNWs 3 nm.

4.2 Effect of Coating and Coating Thickness

The details of the simulation model including two parallel oriented uncoated AgNWs in order to fix the center wavelength value that yields maximum EF are given by Table 4. 9.

Table 4. 9 Center Wavelength Fixing Model for Two Parallel Oriented Uncoated AgNWs

Property	Magnitude (nm)
Radius of Curvature	2
Length of Nanowire	500
Radius	50
Center Wavelength	532, 660, 785
Wavelength Span	100
Distance Btw Rods	5

FDTD analysis results yielding the regarding EFs depending on the three Raman wavelength values are covered by Table 4. 10 yielding the maximum EF for 532 nm that is 3,91E+05.

Table 4. 10 Resulting EFs Depending on Related Three Raman Wavelength Values

Wavelength (nm)	Enhancement Factor
532	3.91E+05
660	2.86E+04
785	6.55E+04

In the following analysis including 4.2.1 the center wavelength is fixed to 532 nm and for 4.2.2 the center wavelength is fixed to 660 nm to observe the effect of TiO_2 thickness on EF.

4.2.1 Parallel Orientation Model

The details of the simulation model including two parallel oriented TiO_2 coated AgNWs are given by Table 4. 11.

Table 4. 11 Parallel Orientation Model for Coating Thickness Analysis (PA=0°)

Property	Magnitude (nm)
Radius of Curvature	2
Length of Nanowire	500
Radius	50
TiO_2 Thickness	0,2,4,6
Center Wavelength	532
Wavelength Span	100
Distance Btw Rods	5

FDTD analysis results yielding the regarding EF's depending on the TiO_2 thickness are covered by Table 4. 12 yielding the maximum EF for 2 nm TiO_2 thickness that is 3,42E+06.

Table 4. 12 Resulting EFs for two parallel oriented TiO_2 coated Samples Depending on TiO_2 Thickness Values

TiO_2 Thickness (nm)	Enhancement Factor
0	2.86E+04
2	3.42E+06
4	6.55E+04
6	2.86E+04

The TiO_2 thickness versus EF graph of TiO_2 coated parallel oriented AgNWs is shown in Figure 4. 4.

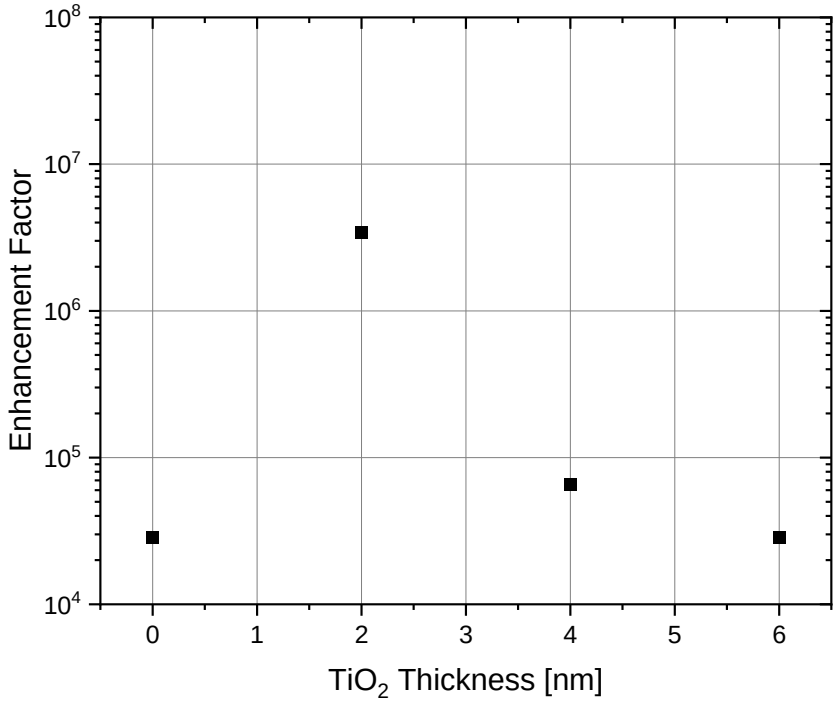

Figure 4. 4 TiO_2 Thickness vs EF Graph of TiO_2 Coated Parallel Oriented AgNWs

4.2.2 Cross Shape Orientation Model

The details of the simulation model including two cross oriented TiO_2 coated AgNWs are given by Table 4. 13.

Table 4. 13 Cross Orientation Model for Coating Thickness Analysis (PA= 0^o, 90^o)

Property	**Magnitude (nm)**
Radius of Curvature	2
Length of Nanowire	500
Radius	50
TiO_2 Thickness	0,2,4,6
Center Wavelength	660
Wavelength Span	100
Distance Btw Rods	5

FDTD analysis results yielding the regarding EFs depending on the TiO_2 thickness are covered by Table 4. 14.

Table 4. 14 Resulting EFs for Cross Oriented Samples Depending on TiO_2 Thickness Values

TiO_2 Thickness (nm)	**EF (PA= 0º)**	**EF (PA= 90º)**
2	6.56E+03	6.55E+04
4	1.46E+04	6.56E+03
6	1.46E+04	2.40E+03

TiO_2 thickness versus EF graph of TiO_2 coated cross oriented AgNWs is illustrated in Figure 4. 5.

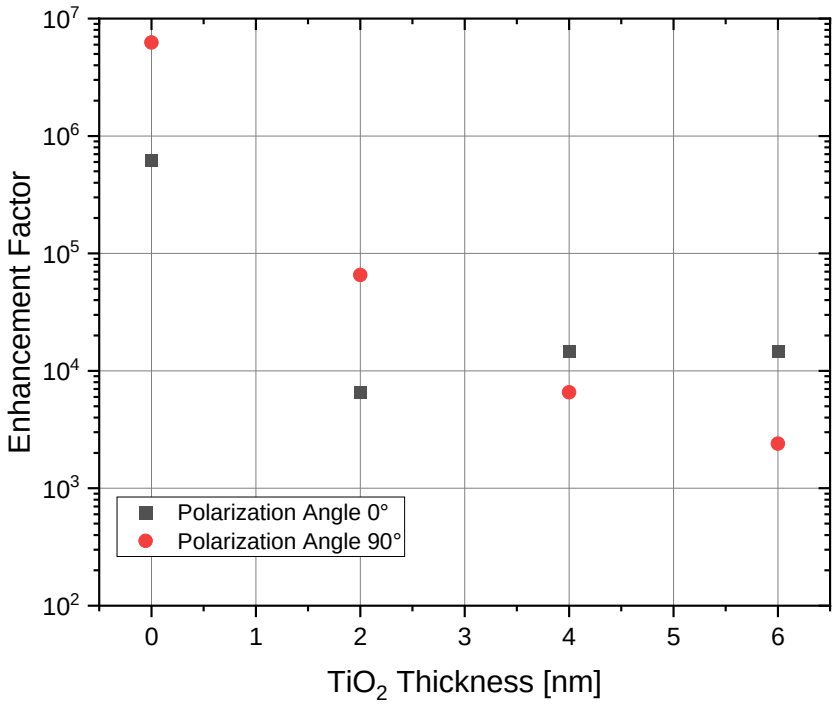

Figure 4. 5 TiO_2 Thickness vs EF Graph of TiO_2 Coated Cross Oriented AgNWs

4.3 Effect of Polarization Angle

4.3.1 Parallel Orientation Model

The details of the simulation model including two parallel oriented TiO_2 coated AgNWs are given by Table 4. 15.

Table 4. 15 Parallel Orientation Model for Polarization Angle Analysis

Property	Magnitude (nm)
Radius of Curvature	2
Length of Nanowire	500
Radius	50
TiO_2 Thickness	2
Center Wavelength	660
Wavelength Span	100
Distance Btw Rods	5

FDTD analysis results yielding the regarding EFs depending on the polarization angle are covered by Table 4. 16.

Table 4. 16 Resulting EFs for Parallel Oriented Samples Depending on Polarization Angle

Polarization Angle (^{o})	Enhancement Factor
0	6.55E+04
30	2.86E+04
45	1.46E+04
60	2.40E+03
90	6.25E+02

Polarization angle versus EF graph of TiO_2 coated parallel oriented AgNWs is illustrated in Figure 4. 6.

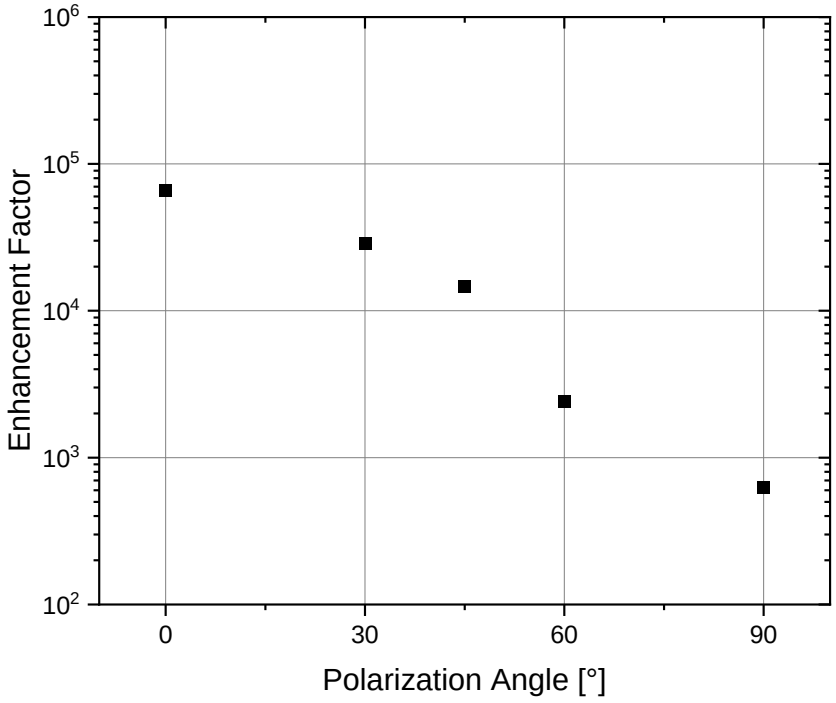

Figure 4. 6 Polarization Angle vs EF Graph of TiO_2 Coated Parallel Oriented AgNWs

FDTD analysis yield that for parallel oriented TiO_2 coated AgNWs the most efficient PA is 0^o that leads to 6.55E+04 EF.

4.3.2 Cross Shape Orientation Model

The details of the simulation model including two cross oriented TiO_2 coated AgNWs are given by Table 4. 17.

Table 4. 17 Cross Orientation Model for Polarization Angle Analysis

Property	**Magnitude (nm)**
Radius of Curvature	2
Length of Nanowire	500
Radius	50
TiO_2 Thickness	2
Center Wavelength	660
Wavelength Span	100
Distance Btw Rods	5

FDTD analysis results yielding the regarding EFs depending on the polarization angle are covered by Table 4. 18.

Table 4. 18 Resulting EFs for Cross Oriented Samples Depending on Polarization Angle

Polarization Angle (º)	**Enhancement Factor**
0	6.56E+03
30	2.40E+03
45	6.56E+03
60	1.46E+04
90	6.55E+04

Polarization angle versus EF graph of TiO_2 coated cross oriented AgNWs is illustrated in Figure 4. 7.

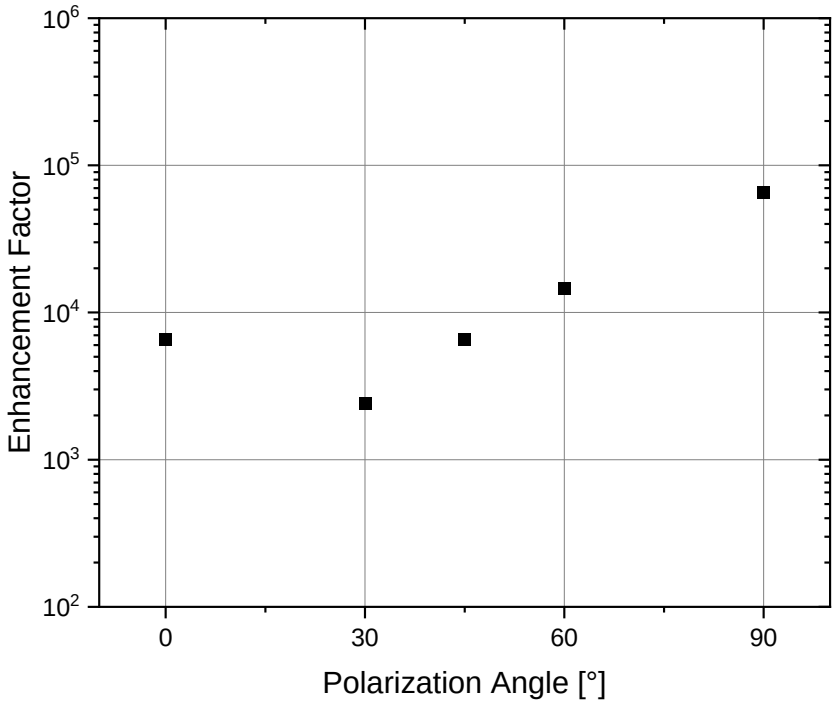

Figure 4. 7 Polarization Angle vs EF Graph of TiO_2 Coated Cross Oriented AgNWs

FDTD analysis yields that for cross oriented TiO_2 coated AgNWs the most efficient PA is 90º that leads to 6.55E+04 EF.

CHAPTER 5

CONCLUSIONS

AgNW filter foils are promising for improving the Raman signal that refers to enhancement mechanism and also for filtering. In the experimental background, AgNWs are synthesized by polyol process that provides control over parameters such as shape, length and diameter. Vacuum filtration method is used to fabricate AgNWs. As a post-treatment PVP is removed in order to prevent the signal interference of PVP and molecule of interest and also to enable the analyte being in close contact with the AgNWs. TiO_2 thin films were deposited on AgNW foils making use of a plasma enhanced ALD (PEALD) system.

Three-dimensional AgNW networks include complex arrangements of wires with various orientations so remarkable number of hot spots that amplifies SERS signal. Taking cross sections and analyzing subsystems through simulations give valuable information about the local enhancements for desired parameters including distance between wires, polarization angle and coating thickness. The photonic and optical simulations make use of boundary element method (BEM), finite element method (FEM) and the finite difference time-domain (FDTD) methods. BEM and FEM methods do not involve time whereas FDTD method provides data regarding time-dependency.

In this thesis, FDTD method is used. Different sub-structures in the random nanowire orientations to be obtained in the experiments are simulated with various probabilities. The metallic nanoparticles due to emergence of surface plasmon resonance produce SERS distinctive enhancement. The enhancement of Raman signal results due to increasing intensity of the electromagnetic field locally. The EF factors of the models are calculated and optimum parameters are defined accordingly.

FDTD analysis yields that for parallel oriented TiO_2 coated AgNWs the most efficient PA is 0^o that leads to 6.55E+04 EF and for cross oriented TiO_2 coated AgNW's the most efficient PA is 90^o that leads to 6.55E+04 EF.

For parallel oriented model the maximum EF is obtained for 2 nm TiO_2 thickness that is 3.42E+06. For cross orientation the polarization angle affects the results; for PA=0^o, 4 nm and 6 nm thickness offer highest EF's that is 1.46E+04 whereas for PA=90^o, 2 nm offers highest EF that is 6.55E+04.

FDTD analysis considering distance dependency of EF yield that for uncoated cross oriented AgNWs the optimum distance is 2 nm with 3.16E+07 EF whereas for TiO_2 coated cross oriented AgNWs the optimum distance is 3 nm with 2.40E+07 EF. For parallel oriented TiO_2 coated AgNWs the optimum distance is 4 nm with 9.23E+05 EF.

The average weight of cross oriented and parallel oriented AgNWs taken from the SEM image (Figure 3. 4) showing the cross section of the foils may be used to estimate a statistical value to represent the EF of whole cross section by making use of subsystem calculations. In the experiments random polarization laser source is used. In the SEM image x direction is chosen as reference to compute statistical EF. The number of parallel, perpendicular and other angled polarization angles that AgNWs experience are determined approximately. For the other angled polarization angles the weight is evenly distributed. The corresponding EF values for desired angle are taken from the simulation results to compute weighted average of the EF value of the network shown in the SEM image. The calculation yields 6.77E+04 EF that is below experimental value. The overall Raman EF estimated from weighted averaging of possible two-wire subsystem configurations is found to be one to two orders of magnitude less than that of the experimentally determined EF of 1E+06 to 1E+07. At first glance this may suggest that two-wire subsystem has limited capacity in representing the AgNW network, however it should be noted that the maximum EFs calculated from particular configurations of two-wire model reaches 1E+07 level. It is an open question if the overall SERS performance should be estimated

from the weighted averages or does the strongest hotspot dominate the overall behavior. Our study can be said to support the latter in this respect.

Using a dielectric material as a thin film on AgNWs previously studied by using Al_2O_3 as coating [103]. The regarding EF calculations in the literature range from 1E+06 to 1E+07 [104]. The coating acts as a tunneling barrier against quantum tunneling effects, optimizes the detection, makes long-time storage possible and may contribute to EF. Using TiO_2 instead of Al_2O_3 is novel and experiments are being carried out concurrently by our research group. In the scope of this work, FDTD analysis yields values ranging from 1E+04 to 1E+07. The variance may be due to the neglection of the contribution of chemical enhancement and due to multiple and multi cross wire effects as simplified two nanowire systems are studied in the simulations. Still multi-parametric analysis is useful to create an optimum set of values to be studied in the experiments and narrowing the range of trials. Moreover, the EF values estimated by FDTD simulations give a reference to compare the effect of desired parameters on EF. As a future work the experimental results and analysis outputs can be compared and discussed in detail. Additional simulation models and parameters can be studied.

REFERENCES

[1] Yu Zhang, Yu-Rong Zhen, Oara Neumann, Jared K Day, Peter Nordlander, and Naomi J Halas. Coherent anti-stokes raman scattering with single-molecule sensitivity using a plasmonic fano resonance. Nature communications, 5(1):1–7 (2014).

[2] C. V. Raman and K. S. Krishnan, "A new type of secondary radiation," *Nature*, vol. 121, no. 3048, pp. 501–502, 1928.

[3] Fleischmann, M.; Hendra, P. J.; McQuillan, A. J. Raman Spectra of Pyridine Adsorbed at a Silver Electrode. Chem. Phys. Lett. 1974, 26, 163−166.

[4] Jeanmaire, D. L.; Van Duyne, R. P. Surface Raman Spectroelectrochemistry Part I. Heterocyclic, Aromatic, and Aliphatic Amines Adsorbed on the Anodized Silver Electrode. J. Electroanal. Chem. Interfacial Electrochem. 1977, 84, 1−20.

[5] Albrecht, M. G.; Creighton, J. A. Anomalously Intense Raman Spectra of Pyridine at a Silver Electrode. J. Am. Chem. Soc. 1977, 99, 5215−5217.

[6] Philpott, M. R. Effect of Surface Plasmons on Transitions in Molecules. J. Chem. Phys. 1975, 62, 1812.

[7] Moskovits, M. Surface Roughness and the Enhanced Intensity of Raman Scattering by Molecules Adsorbed on Metals. J. Chem. Phys.1978, 69, 4159.

[8] K. Kneipp, H. Kneipp, I. Itzkan, R. P. Dasari, and M. S. Feld, "Surface-enhanced Raman scattering and biophysics," *J. Phys. Condens. Matter*, vol. 14, no. 18, pp. R597–R624 (2002).

[9] Harry A Atwater. The promise of plasmonics. Scientific American, 296(4):56–63 (2007).

[10] Jeon, T.Y.; Kim, D.J.; Park, S.-G.; Kim, S.-H.; Kim, D.-H. Nanostructured plasmonic substrates for use as SERS sensors. Nano Converg. 2016, 3, 1–20.

[11] Dong, H., Wu, Z., Gao, Y., El-Shafei, A., Jiao, B., Dai, Y., & Hou, X. (2014). A nanostructure-based counter electrode for dye-sensitized solar cells by assembly of silver nanoparticles. Organic Electronics, 15(7), 1641–1649.

[12] F. L. Pedrotti, L. S. Pedrotti, and L. M. Pedrotti, Introduction to Optics, 3rd ed. (2007).

[13] Richard P. Feynman, Robert B. Leighton, and Matthew Sands, The Feynman Lectures on Physics, vol. 1 (Reading, Mass.: Addison-Wesley Publishing Company, 1963), Ch. 32, 33.

[14] McGregor, Hanna & Wang, Wenbo & Short, Michael & Zeng, Haishan. (2016). Clinical utility of Raman spectroscopy: current applications and ongoing developments. Advanced Health Care Technologies. 13. 10.2147/AHCT.S96486.

[15] P. L. Stiles, J. A. Dieringer, N. C. Shah, and R. P. Van Duyne, "Surface-enhanced Raman spectroscopy," Annu. Rev. Anal. Chem., vol. 1, no. 1, pp. 601–626 (2008).

[16] Lindon, J. C., Tranter, G. E., & Koppenaal, D. W. *Encyclopedia of spectroscopy and spectrometry*. Elsevier (2017).

[17] P. Vandenabeele, Practical Raman Spectroscopy. Wiley (2013).

[18] Downes, A., & Elfick, A. (2010). Raman spectroscopy and related techniques in biomedicine. Sensors, 10(3), 1871–1889.

[19] Quiño, J., Ruehl, M., Klima, T., Ruiz, F., Will, S., & Braeuer, A. (2016). Supercritical drying of aerogel: In situ analysis of concentration profiles inside the gel and derivation of the effective binary diffusion coefficient using Raman spectroscopy. *The Journal of Supercritical Fluids*, *108*, 1–12.

[20] Paul R West, Satoshi Ishii, Gururaj V Naik, Naresh K Emani, Vladimir M Shalaev, and Alexandra Boltasseva. (2010) Searching for better plasmonic materials. Laser & Photonics Reviews, 4(6):795–808.

[21] Harry A Atwater. (2007) The promise of plasmonics. Scientific American, 296(4):56– 63.

[22] Abbe, E. (1873) Beitr€age zur Theorie des Mikroskops und der mikroskopischen Wahrnehmung. Arch. Mikroskop. Anat. 9(1): 413–418.

[23] Synge, E.H. (1928) 'A suggested method for extending the microscopic resolution into the ultramicroscopic region', The London, Edinburgh, and Dublin Philisophical Magazine and J. Sci., Vol. 6, pp.356.

[24] Ash, E. A., and G. Nicholis. (1972) 'Super-resolution aperture scanning microscope', Nature (*Lond*.). 237:510.

[25] Lewis, A., Isaacson, M., Harootunian, A. and Murray, A. (1984) 'Development of a 500A spatial resolution light microscope', Ultramicroscopy, Vol. 13, pp.227.

[26] Murray, A., Isaacson, M., Adesida, I. and, Whitehead, J. (1983) 'Fabrication of apertures, slots, and grooves at the 8-80 nm scale in silicon and metal films', J. Vac. Sci. Technol., Vol. 1, pp.1091.

[27] Pohl, D.W., Denk, W. and Lanz, M. (1984) 'Optical stethoscopy: image recording with resolution lambda/20', Appl. Phys. Lett., Vol. 44, pp.651.

[28] Reddick, R.C., Warmack, R.J. and Ferrell, T.L. (1989) 'New form of scanning optical microscopy', Phys. Rev. B, Vol. 39, pp.767.

[29] Vigoureux, J.M., Girard, C. and Courjon, D. (1989) 'General principles of scanning tunnelling optical microscopy', Opt. Lett., Vol. 14, pp.1039.

[30] Betzig, E., Finn, P.L. and Weiner, J.S. (1992) 'Combined shear force and near-field scanning optical microscopy', Appl. Phys. Lett., Vol. 60, pp.2484.

[31] Ruiter, A.G.T., van der Werf, K.O., Veerman, J.A., Garcia-Parajo, M.F., Rensen, W.H.J. and van Hulst, N.F. 'Tuning fork shear-force feedback', Ultramicroscopy, Vol. 71, pp.149 (1998).

[32] Antognozzi, M., Szczelkun, M.D., Round, A.N. and Miles, M.J. 'Comparison between shear force and tapping mode AFM – High resolution imaging of DNA', Single Mol., Vol. 3, pp.105 (2002).

[33] Wetsel, G.C., Farahi, R.H., Richardson, C.J.K. and Spicer, J.B. 'Approach interactions of scanned probes in dynamic pecking mode', Appl. Phys. Lett., Vol. 79, pp.2657 (2001).

[34] Lieberman, K. and Lewis, A. 'Simultaneous scanning tunnelling and optical near-field imaging with a micropipette', Appl. Phys. Lett., Vol. 62, pp.1335 (1993).

[35] Garcia-Parajo, M., Cambril, E. and Chert, Y. 'Simultaneous scanning tunnelling microscope and collection mode scanning near-field optical microscope using gold coated optical fiber probes', Appl. Phys. Lett., Vol. 65, pp.1498 (1994).

[36] Puygranier, B.A.F. and Dawson, P. 'Chemical etching of optical fibre tips – experiment and model', Ultramicroscopy, Vol. 85, pp.235 (2000).

[37] Ohtsu, M. 'Photon STM: from imaging to fabrication', Optoelectron.-Devices Technol., Vol. 10, pp.147 (1995).

[38] Valaskovic, G.A., Holton, M. and Morrison, G.H. 'Parameter control, characterization and optimization in the fabrication of optical fiber near-field probes', Appl. Opt., Vol. 34, pp.1215 (1995).

[39] Yakobson, B.I. and Paesler, M.A. 'Kinetics, morphology and pulling regimes for sensing tips in near-field microscopy', Ultramicroscopy, Vol. 57, pp.241 (1995).

[40] Garcia-Parajo, M., Tate, T. and Chen, Y. 'Gold-coated parabolic tapers for scanning near field optical microscopy: fabrication and optimisation', Ultramicroscopy, Vol. 61, pp.155 (1995).

[41] B. E. A. Saleh and M. C. Teich, Fundamentals of Photonics, 1st ed. New York: Wiley (1991).

[42] J. Li and N. Wu, "Biosensors Based on Nanomaterials and Nanodevices," CRC Press (2013).

[43] H. Qi, R. W. Rendell, O. J. Glembocki and S. M. Prokes, J. Nanomater., 2012, 2012, 1–10.

[44] I. R. Lewis and H. Edwards, Handbook of Raman spectroscopy–from the research laboratory to the process line, CRC Press (2001).

[45] Raman Imaging: Techniques and Applications, ed. A. Zoubir, Springer (2012).

[46] M. Culha, B. Cullum, N. Lavrik and C. K. Klutse, J. Nanotechnol., 2012, 1–15.

[47] Guo, H., He, L., & Xing, B.Applications of surface-enhanced Raman spectroscopy in the analysis of nanoparticles in the environment. *Environmental Science: Nano*, 2017, *4*(11), 2093–2107.

[48] Kathryn M Mayer and Jason H Hafner. Localized surface plasmon resonance sensors. Chemical reviews, 111(6):3828–3857 (2011).

[49] Tay LL. Surface Plasmons (2016).

[50] S. A. Maier, Plasmonics : Fundamentals and Applications. New York: Springer (2007).

[51] I. Long, G. Mie, and R. Ritchie, Plasmonics (1957).

[52] R. H. Ritchie, Phys. Rev., 106, 874 (1957)

[53] Nazarov, M., Noh, D. Y., Arellano, I., & Lee, S. W. (2009). Infrared and Raman spectroscopy of double activated YNbO4:Eu3+,Tb3+. 2009 34th International Conference on Infrared, Millimeter, and Terahertz Waves.

[54] Katherine A Willets and Richard P Van Duyne. Localized surface plasmon resonance spectroscopy and sensing. Annu. Rev. Phys. Chem., 58:267–297 (2007).

[55] Zeng, Y., Hu, R., Wang, L., Gu, D., He, J., Wu, S. Y., et al. Recent advances in surface plasmon resonance imaging: detection speed, sensitivity, and portability. Nanophotonics, 2017, 6(5), 1017-1030.

[56] Li, g. Nano-inspired biosensors for protein assay with clinical applications. Elsevier (2019).

[57] R. J. Newhouse and J. Z. Zhang, "Optical properties and applications of shape-controlled metal nanostructures," in Reviews in Plasmonics, C. D. Geddes, Ed. Springer, 2012, pp. 205–238.

[58] Brongersma and Pieter G Kik. Surface plasmon nanophotonics, volume 131. Springer (2007).

[59] JM Pitarke, VM Silkin, EV Chulkov, and PM Echenique. Theory of surface plasmons and surface-plasmon polaritons. Reports on progress in physics, 70(1):1, (2006).

[60] Eleonora Petryayeva and Ulrich J Krull. Localized surface plasmon resonance: Nanostructures, bioassays and biosensing—a review. Analytica chimica acta, 706(1):8–24 (2011).

[61] E. C. Le Ru and P. Etchegoin, Principles of Surface Enhanced Raman Spectroscopy, 1st ed. Amsterdam: Elsevier (2009).

[62] Joseph M Luther, Prashant K Jain, Trevor Ewers, and A Paul Alivisatos. Localized surface plasmon resonances arising from free carriers in doped quantum dots. Nature materials, 10(5):361–366 (2011).

[63] P. G. Etchegoin and E. C. Le Ru, "Basic electromagnetic theory of SERS," in Surface Enhanced Raman Spectroscopy: Analytical, Biophysical and Life Science Applications, S. Schlücker, Ed. Weinheim: Wiley-VCH, 2011, pp. 1– 37.

[64] L. Novotny and B. Hecht, Principles of Nano-Optics, 1st ed. Newyork: Cambridge (2006).

[65] Robin R Jones, David C Hooper, Liwu Zhang, Daniel Wolverson, and Ventsislav K Valev. Raman techniques: fundamentals and frontiers. Nanoscale research letters, 14(1):1–34 (2019).

[66] Lombardi, J. R., Birke, R. L. A unified approach to surface-enhanced Raman spectroscopy. The Journal of Physical Chemistry C, 112(14), 5605–5617 (2008).

[67] Meikun Fan, Gustavo F.S. Andrade, Alexandre G. Brolo, A review on the fabrication of substrates for surface enhanced Raman spectroscopy and their applications in analytical chemistry, Analytica Chimica Acta, Volume 693, Issues 1–2, 2011, 7-25.

[68] M. Fleischmann, P.J. Hendra, A.J. McQuillan, Journal of the Chemical SocietyChemical Communications (1973) 80.

[69] B. Pettinger, U. Wenning, H. Wetzel, Surface Science 101 (1980) 409.

[70] Pilot, R., Signorini, R., Durante, C., Orian, L., Bhamidipati, M. and Fabris, L. A Review on Surface-Enhanced Raman Scattering, 9, 57 (2019).

[71] Brown, R.J.C., Milton, M.J.T. Nanostructures and nanostructured substrates for surface-enhanced Raman scattering (SERS). J. Raman Spectrosc. 2008, 39, 1313–1326.

[72] Hakonen, A., Andersson, P.O., Stenbæk Schmidt, M., Rindzevicius, T. and Käll, M. Explosive and chemical threat detection by surface-enhanced Raman scattering: A review. Anal. Chim. Acta 2015, 893, 1–13.

[73] Zheng, J., He, L. Surface-Enhanced Raman Spectroscopy for the Chemical Analysis of Food. Compr. Rev. Food Sci. Food Saf. 2014, 13, 317–328

[74] Bonifacio, A., Cervo, S. and Sergo, V. Label-free surface-enhanced Raman spectroscopy of biofluids: Fundamental aspects and diagnostic applications. Anal. Bioanal. Chem. 2015, 407, 8265–8277.

[75] Lane, L.A., Qian, X. and Nie, S. SERS Nanoparticles in Medicine: From Label-Free Detection to Spectroscopic Tagging. Chem. Rev. 2015, 115, 10489–10529.

[76] Hamm, L., Gee A. and Indrasekara, A. S. Recent advancement in the surface-enhanced Raman spectroscopy-based biosensors or infectious disease diagnosis. Applied Sciences, 9(7), 1448.

[77] Su, X.; Zhang, J.; Sun, L.; Koo, T.; Chan, S.; Sundararajan, N.; Yamakawa, M.; Berlin, A.A. Composite Organic—Inorganic Nanoparticles (COINs) with Chemically Encoded Optical Signatures. Nano Lett. 2005, 5, 49–54.

[78] Fabris, L. Gold-based SERS tags for biomedical imaging. J. Opt. 2015, 17, 114002.

[79] Kang, T.; Yoo, S.M.; Yoon, I.; Lee, S.Y.; Kim, B. Patterned Multiplex Pathogen DNA Detection by Au Particle-on-Wire SERS Sensor. Nano Lett. 2010, 10, 1189–1193.

[80] Shanmukh, S.; Jones, L.; Driskell, J.; Zhao, Y.; Dluhy, R.; Tripp, R.A. Rapid and sensitive detection of respiratory virus molecular signatures using a silver nanorod array SERS substrate. Nano Lett. 2006, 6, 2630–2636.

[81] Xu, L.J.; Zong, C.; Zheng, X.S.; Hu, P.; Feng, J.M.; Ren, B. Label-free detection of native proteins by surface-enhanced Raman spectroscopy using iodide-modified nanoparticles. Anal. Chem. 2014, 86, 2238–2245.

[82] Efrima, S.; Bronk, B.V. Silver Colloids Impregnating or Coating Bacteria. J. Phys. Chem. B 1998, 102, 5947–5950.

[83] Xu, B.-B.; Ma, Z.-C.; Wang, L.; Zhang, R.; Niu, L.-G.; Yang, Z.; Zhang, Y.-L.; Zheng, W.-H.; Zhao, B.; Xu, Y.; et al. Localized flexible integration of high-efficiency surface enhanced Raman scattering (SERS) monitors into microfluidic channels. Lab Chip 2011, 11, 3347–3351.

[84] Lereu, A.L., Passian, A. and Dumas, Ph. (2012) 'Near field optical microscopy: a brief review', Int. J. Nanotechnol., Vol. 9, Nos. 3–7, pp.488–501.

[85] Pilot, R.; Signorini, R.; Fabris, L. Surface-Enhanced Raman spectroscopy: Principles, Substrates, and Applications. In Metal Nanoparticles and Clusters: Advances in Synthesis, Properties and Applications; Deepak, F.L., Ed.; Springer: Cham, Switzerland, 2018; pp. 89–164.

[86] Ding, S.-Y.; You, E.-M.; Tian, Z.-Q.; Moskovits, M. Electromagnetic theories of surface-enhanced Raman spectroscopy. Chem. Soc. Rev. 2017, 46, 4042–4076.

[87] Kleinman, S.L.; Frontiera, R.R.; Henry, A.-I.; Dieringer, J.A.; Van Duyne, R.P. Creating, characterizing, and controlling chemistry with SERS hot spots. Phys. Chem. Chem. Phys. 2013, 15, 21–36.

[88] Jensen, L.; Aikens, C.M.; Schatz, G.C. Electronic structure methods for studying surface-enhanced Raman scattering. Chem. Soc. Rev. 2008, 37, 1061.

[89] Aroca, R. Surface-Enhanced Vibrational Spectroscopy; John Wiley & Sons, Ltd.: Chicester, UK, 2006.

[90] M. L. Weber and K. a. Willets, “Nanoscale studies of plasmonic hot spots using super-resolution optical imaging,” MRS Bull., vol. 37, no. 8, pp. 745– 751 (2012).

[91] Fl J García-Vidal and JB Pendry. Collective theory for surface enhanced raman scattering. Physical Review Letters, 77(6):1163 (1996).

[92] E. C. Le Ru, M. Meyer, P. G. Etchegoin, and E. Blackie, “Surface enhanced Raman scattering enhancement factors: a comprehensive study,” J. Phys. Chem. C, vol. 111, no. 37, pp. 13794–13803 (2007).

[93] M. D. Sonntag, J. M. Klingsporn, A. B. Zrimsek, B. Sharma, L. K. Ruvuna, and R. P. Van Duyne, “Molecular plasmonics for nanoscale spectroscopy,” Chem. Soc. Rev., vol. 43, no. 4, pp. 1230–47 (2014).

[94] Long, D.A. The Raman Effect a Unified Treatment of the Theory of Raman Scattering by Molecules; Wiley: Chichester, UK, 2002; ISBN 9780471490289.

[95] Dennis M. Sullivan, Electromagnetic simulation using the FDTD method. New York: IEEE Press Series (2000).

[96] Allen Taflove, Computational Electromagnetics: The Finite-Difference Time-Domain Method. Boston: Artech House (2005).

[97] Stephen D. Gedney, Introduction to the Finite-Difference Time-Domain (FDTD) Method for Electromagnetics. Morgan & Claypool publishers (2011).

[98] K.S. Yee, "Numerical solution of initial boundary value problems involving Maxwell's equations in isotropic media" IEEE Trans. Antennas Propagat., AP-14, 302 (1966).

[99] K.S. Yee, IEEE Trans. Antennas and Propagation, Vol. 14, 1966, pp. 302–307, © 1966 IEEE.

[100] B. Sharma, R. R. Frontiera, A. I. Henry, E. Ringe, and R.P. Van Duyne, " SERS: materials, applications, and the future," *Materials Today*, vol. 15, no. 1-2, pp 16-25 (2012).

[101] C.B. Moore, W. Rison, J. Mathis, and G. Aulich, "Lightning rod improvement studies," *Journal of Applied Meteorology*, vol. 39, no. 5, pp. 593-609 (2000).

[102] Coskun, S., Aksoy, B. and Unalan, H. E., "Polyol Synthesis of Silver Nanowires: An Extensive Parametric Study," Cryst. Growth Des. 11(11), 4963–4969 (2011).

[103] Demirtas, Ö., Akdemir, O., Coşkun, Ş., Ünalan, H. E. and Bek, A. "Multifunctional, flexible, and free-standing sers-active AgNW filter foils," Nanophotonics VIII (2020).

[104] Y. Ma, J. Zhou, W. Zou, Z. Jia, L.Petti, and P.Mormile, "Localized surface plasmon resonance and surface enhanced raman scattering responses of Au@Ag core-shell nanorods with different thickness of Ag shell," Journal of Nanoscience and Nanotechnology, vol. 14, no.6, pp. 4245-4250 (2014).

[105] H. Oğuz, “Development of SERS-active silver nanowire filter foils for pathogen detection in fluids,” M.S. - Master of Science, Middle East Technical University (2022).